Heavy ion radiolysis of the chiral terpene α-pinene

A L. F. de Barros, A. Ricca, A. Bychkova, C A. P. da Costa, J. W. Costa, P. Boduch, H. Rothard, E. F. da Silveira, Alicja Domaracka

To cite this version:

A L. F. de Barros, A. Ricca, A. Bychkova, C A. P. da Costa, J. W. Costa, et al.. Heavy ion radiolysis of the chiral terpene α-pinene. Monthly Notices of the Royal Astronomical Society, 2024, pp.stae757. 10.1093/mnras/stae757 . hal-04516709

Heavy ion radiolysis of the chiral terpene α-pinene

A. L. F. de Barros[1,4], A. Ricca[2,3], A. Bychkova[4], C. A. P. da Costa[4], J. W. Costa[1], P. Boduch[4], H. Rothard[4], E. F. da Silveira[5], A. Domaracka[4]
[1] *Departamento de Física, Centro Federal de Educação Tecnológica Celso Suckow da Fonseca, Av. Maracanã 229, 20271-110 Rio de Janeiro, RJ, Brazil*
[2] *Carl Sagan Center, SETI Institute, 339 Bernardo Ave., Suiote 200, Mountain View, CA 94043, USA*
[3] *NASA Ames Research Center, Mail Stop 245-6, Moffett Field, CA 94035-1000, USA*
[4] *Centre de Recherche sur les Ions, les Matériaux et la Photonique Normandie Univ, ENSICAEN, UNICAEN, CEA, CNRS, CIMAP, 14000 Caen, France*
[5] *Departamento de Física, Pontifícia Universidade Católica do Rio de Janeiro, Rua Marquês de São Vicente 225, 22451-900, Rio de Janeiro, RJ, Brazil*

Received

ABSTRACT

Radiolysis of α-pinene by 61.3 MeV ^{84}Kr^{15+} ions is analyzed, with the scope to simulate the effects produced by heavy ion cosmic ray bombardment in typical interstellar medium. The α-pinene ice samples were irradiated at 10 K and their chemical evolution was monitored by mid-infrared Fourier transform (FTIR) spectroscopy to characterize the reaction products and to determine the extent of racemization. The integrated band strengths have been obtained for all the neutral α-pinene vibrational bands using the experimental band integrated absorbances and the theoretical absolute intensities calculated along the column densities. In the current heavy ion bombardment experiments, small molecules were formed and the precursor, α-pinene, was destroyed instead of being racemized. Twelve hydrocarbons were produced (final fluence of 2.0×10^{12} ions.cm^{-2}): methane (CH_4), acetylene (C_2H_2), ethylene (C_2H_4), propylene (C_3H_6), propane (C_3H_8), n-butane (C_4H_{10}), butene (C_4H_8), propyne (C_3H_4), benzene (C_6H_6), ethane (C_2H_6), vinylacetylene (C_4H_4) and 2-methyl-1,3-butadiene or isoprene (C_5H_8). The highest formation cross section ($\sim 40 \times 10^{-15}$ cm^2) was observed for the C_3H_4 and the lowest is C_3H_8 ($\sim 3 \times 10^{-15}$ cm^2). The radiochemical yields for these molecules follow the same trends as those of their cross sections. The atom budget calculation confirms that all the expected products have been generated during the radiolysis and supports the conclusion that the proposed A-values are accurate. The α-pinene sputtering yield for this ion beam was found to be $Y_0 = 1.84 \times 10^6$ molecules per impact.

Key words: astrochemistry – methods: laboratory: solid state – astronomical instrumentation, methods and techniques: spectroscopic – Interstellar medium (ISM), nebulae: cosmic rays.

1 INTRODUCTION

A chiral molecule is a molecule that is nonsuperimposable on its mirror image, and is chemically distinct from the molecule represented by its mirror image. Chiral molecules contain one or more chiral centers; these molecules constitute the foundation of the biochemistry of the biological world. As a result, the chirality of molecules and macromolecules is directly related to life Cataldo et al. (2007a); Cataldo & Iglesias-Groth (2017). Without chirality, life cannot be envisioned since it would be impossible to carry out the complicated chemistry and biology necessary for living things to exhibit great selectivity in chemical reactions Cataldo et al. (2007a); Cataldo (2007b,c).

According to Lord Kelvin's definition from 1904, chirality is the property that prevents an object from being superimposable onto its mirror image. Chirality is a significant 3D structural attribute that is highly significant in the fields of chemistry and biological sciences at the molecular level(Bonner 1991; Guijarro & Yus 2008). Specifically, chiral species include the building blocks of proteins, sugars found in nucleic acids, and amino acids, which are the building blocks of life (Nahon et al. 2007; Hadidi et al. 2018). Additionally, these biomolecules are found in the biosphere as homochiral species (Darquie et al. 2010; Guijarro & Yus 2008), and their handedness dictates that of related biopolymers like DNA and protein alpha helices (Hadidi et al. 2018).

Comets and meteorites contain prebiotic organic compounds that are integrated from the Solar Nebula. Since these bodies are so far from the Sun, it is generally believed that they get very little UV light and that none of them undergo significant thermal processing (Ehrenfreund et al. 2001, 2007; Tia et al. 2013; Thakur & Remsing 2023). Because of this, the organic material trapped in cometary bodies doesn't change from its basic state. Cosmic rays and the naturally occurring radionuclide decay in the body's mineral rocks are the reasons behind the processing (Cataldo 2007c; Closs et al. 2020, 2022).

In the many settings of the ISM and in our Solar System, isoprene and its oligomers, terpenes, for example: α-pinene and β-pinene, are anticipated to exist alongside more complex organic compounds (Cataldo & Ursini 2011; Cataldo & Iglesias-Groth 2017). It has been difficult to identify and comprehend the significance of these compounds since there is little spectrum data for these molecules at lower temperatures.

Cataldo (2007c) and his research group have study the radiolysis of chiral terpenes has involved α(-)pinene, α(+)pinene and β(-)pinene under a radiation exposure of up to 14,000 kGy gamma radiation, in a way to understand the action of cosmic rays on the surface of comets and meteorites, including understanding their causes under complete radiation processing of the surface of these bodies. The terpene β(-)pinene was a special exception because it proceeds via radiation-induced polymerization rather than the anticipated radioracemization process. For the terpenes α(+)pinene, α(-)pinene they were radiolyzed at radiation doses of 150, 300 and 600 kGy (Cataldo 2007b). The radiolysis of the other enantiomer, α(-)pinene, produces the same chromatograms and the same products of α(+)pinene, and they verified that both α(-)pinenes racemize almost linearly with the amount of the administered radiation dose.

Cataldo (2007b) verified that the chirality is not preserved when high-energy radiation interacts with primitive chiral compounds. Chiral molecules that are part of comets and meteorites are subjected to billions of years of radiation from cosmic rays and high-energy radiation from naturally occurring radionuclide decay (Cataldo 2007b). The entire radiation processing of comets and meteorites' surfaces is caused by the action of cosmic rays on their surface; however, below about 20 meters, the cosmic rays are entirely attenuated, and the radiation should only arise from radionuclide decay.

The action of high-energy radiation on prebiotic chiral molecules plays against the preservation of chirality. Chiral molecules incorporated in comets and meteorites are bombarded for billions of years by cosmic rays and by the high-energy radiation due to the decay of naturally occurring radionuclides. Chiral molecules, such as α-pinene, have been proposed as a potential biological marker for the existence of life on distant planets and exoplanets in astrophysics Zhang et al. (2021); Ramachandran et al. (2022). Based on a comparison of the aliphatic absorption characteristic of α-pinene dust analogs with that of the reported ISM absorption spectra, Günay et al. (2018) produced isoprene based interstellar dust analogs in the laboratory and proposed isoprene as a suitable candidate component of the interstellar dust. Even though increasingly complex organic compounds are being found in astrophysical surroundings, isoprene and terpenes have proven to be quite elusive in astronomical studies thus far. However, there is a greater chance of finding them soon with the high resolution James Webb Space Telescope (JWST) in development.

An et al. (2016) made an-depth analysis of the Raman and IR spectra of non-irradiated isoprene, terpenoids, pinenes, and their mixtures at room temperature. Their results revealed distinct inherent vibrational spectroscopic signatures for each of these compounds. First-principles calculations of the Raman and infrared activities were also carried out for reference. It is remarkable to notice that the experimental spectra agree peak-to-peak with the vibrational activity predicted by DFT (Density Functional Theory). However, they did not calculated the A-values for α-pinene.

Ramachandran et al. (2022) conducted some experiments in vacuum ultraviolet (VUV) photoabsorption studies on pure molecular ices of isoprene and a few basic terpenes, including limonene, α-pinene, and β-pinene. They provide for the first a low temperature (10 K) VUV spectra of isoprene and its oligomers limonene, α-pinene and β-pinene. With the exception of isoprene, whose ice phase absorption shows a noticeable red shift, all of the compounds given here's VUV photoabsorption spectra show similarities in the ice and gas phases as predicted. Isoprene's exceptional absorption at longer wavelengths and its special feature make it a good candidate for detection on frozen substances.

Because of the lack experiments with chirality compounds, and the knowledge that complex molecule observations in comets and in star-forming areas show the presence of effective prebiotic formation processes Guijarro & Yus (2008); Cataldo & Iglesias-Groth (2017). The fact that most ices are mixed in astrophysical environments complicates the chemistry. Thus, it is necessary to have a quantitative knowledge of how various mixture ingredients influence the ice astrochemistry in order to predict the result of ice irradiation in space.

This research focuses on the impact of pure α-pinene ice irradiated with $^{84}\mathrm{Kr}^{15+}$ heavy ion irradiation due to its prominence and known effects on the ice binding environment. These kind of experiments are used to probe the fundamental principles of ice astrochemistry, which can then be applied to more complex ice systems through a combination of modeling and additional experiments. They are not intended to perfectly mimic the multicomponent ice mixtures found in space, but will help to understand the chemistry related of this molecule during heavy ion collisions. Therefore, in order to facilitate their identification in space, a comprehensive spectrum profile of these compounds under such astrophysical settings is required. It was for the first time that α-pinene was irradiated with heavy ions. The spectra in the mid-infrared (MIR) (4000 - 600 cm^{-1}) region was determine at 10 K during irradiation. We determine the α-pinene band strengths and following the evolution of the IR bands of identified radiolysis products as a function of irradiation fluence. Theoretical data are used to interpret laboratory the α-pinene spectra and help identify the formed product bands. Their importance into understand the nature and quantity of organic molecules in space, and the requirement of information of their survival duration's (or decomposition rates). In this work we discuss the possible contribution of the organic compounds α-pinene related their formed products and determine their formation and destruction cross sections. It is expected, with the results, to contribute to understand how organic molecules, that are mostly destroyed in space by UV photolysis, how they behave during a cosmic ray bombardment, like the heavy ion simulated in this work.

2 EXPERIMENTAL PROCEDURES

The experiments were conducted using the IGLIAS set-up of CIMAP-CIRIL ("Centre de recherche sur les Ions, Matériaux et la Photonique") inside a high vacuum chamber (10^{-8} mbar) at the IRRadiation SUD (IRRSUD) beamline of the French National Heavy Ion Accelerator (GANIL). More information is also available in de Barros et al. (2011a,b). It is well known that krypton, iron, and nickel ions are relatively

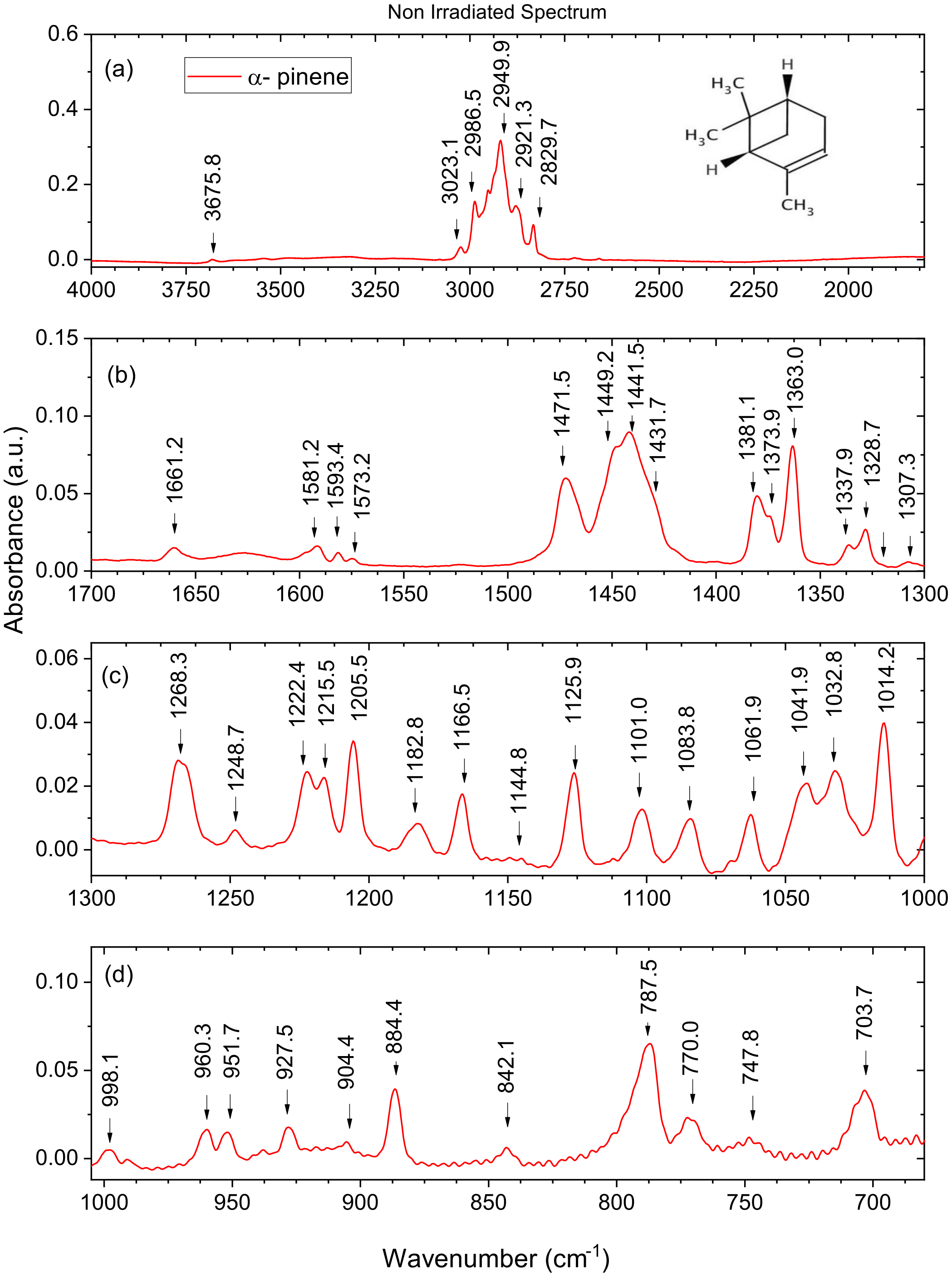

Figure 1. Measured infrared band positions of non-irradiated α-pinene at 10 K. (a) from 4000 to 1800 cm^{-1} wavenumbers; (b) from 1700 to 1300 cm^{-1}; (c) from 1300 to 1000 cm^{-1} and (d) from 1005 to 650 cm^{-1}.

abundant heavy ion cosmic-ray components, roughly 2.2×10^{-4} with respect to protons (Tanabashi et al. 2018). In this work, α-pinene ($C_{10}H_{16}$; structure is presented in Fig.1) is irradiated with 61.3 MeV $^{84}Kr^{15+}$ ion beam. Usually, the average radiolysis effects of heavy ions may be up to 10^3 times greater than those of protons (de Barros et al. 2011b; Mejía et al. 2013).

Fourier Transform Infrared Spectroscopy (FTIR) was used in transmission mode to track evolution of column densities as a function of beam fluence (the total number of projectiles per surface area irradiating the sample) Augé et al. (2018). Spectra in the mid-IR region were collected with Bruker Vertex 70v spectrometer with a specific range of 4000-600 cm^{-1}, a spectral resolution of 2 cm^{-1}, and an average of 70 scans. Infrared spectra are collected at 12^o of incidence to allow a simultaneous recording while the sample is irradiated at normal incidence with the ions provided by the GANIL beam.

α-pinene films were deposited on ZnSe substrates at a temperature of 10 K. A commercially available α-pinene sample was purified before using a series of freeze-pump-thaw cycles to get rid of air and other contaminants that are volatiles above the liquid N_2 temperature. The α-pinene was a 98.8% pure liquid from Sigma Aldrich. Then, α-pinene vapors were injected to a pre-chamber that had been evacuated to a pressure of 10^{-6} mbar. The background pressure before the deposition in the IGLIAS main chamber was 10^{-10} mbar. The full spectrum of a non-irradiated α-pinene from 4000 to 650 cm^{-1} is shown in Fig 1.

The Kr bombardment was performed at almost normal incidence on the α-pinene ice films. The electronic and nuclear energy rates transferred per projectile via electronic interaction are around $S_e = 6.13 \times 10^3$ keV μm^{-1} and $S_n = 2.29 \times 10^1$ keV μm^{-1}, respectively, values obtained by SRIM code (Ziegler et al. 2010). The range of these projectiles is 18.9 μm in this target, more than sufficient to traverse completely the 10.5 μm thickness of the ice layer. The thickness, η, of the α-pinene was determined by Eq.(1) in microns:

$$\eta = \frac{N_0 M 10^4}{\rho N_A} \tag{1}$$

where: N_0 is the initial column density of the ice, M is the total molecular mass, N_A Avogadro constant, and ρ is the α-pinene density (0.858 g.cm^{-3}) (Kramida et al. 2012).

3 THEORETICAL METHODS

The geometry optimizations and the harmonic frequency calculations were performed using density functional theory (DFT). We used the hybrid B3LYP functional (Becke 1993; Stephens et al. 1994) with the cc-pVTZ basis set (Dunning 1989) and the Gaussian 16, Revision A.03 suite of programs (Frisch et al. 2016). The computed harmonic frequencies were scaled to lower frequencies by using the following three scale factors: 0.9750 for bands between 0-1111 cm^{-1}, 0.9790 for bands between 1111-2500 cm^{-1}, and 0.9640 for bands with frequencies >2500 cm^{-1} (Bauschlicher et al. 2018). The integrated band intensities were broadened by 7 cm^{-1} to produce synthetic spectra with band widths comparable with experimental ones. Fig.2 presents a comparison between the experimental IR spectrum with the theoretical spectrum calculated for neutral α-pinene in the region of the most intense bands. Table 1 displays all positions of bands in the MIR (600 to 2000 cm^{-1}) region (in cm^{-1} and μm), the A-values (km mol^{-1}), and the theoretical absolute band positions (cm^{-1}) determined in this work, with the absolute intensities (km mol $^{-1}$), the symmetry from theory, and assignments applying a cut-off for A-values < 2 km mol $^{-1a}$.

4 RESULTS AND DISCUSSION

4.1 Non-irradiated neutral $\alpha-$pinene

A comparison, presented in Fig.2, between the experimental non-irradiated mid-infrared spectrum of α-pinene (shown in red) and the computed mid-infrared spectrum (shown in blue) of neutral α-pinene, shows that the experimental band profiles are well reproduced by theory in the whole spectral range although some theory bands are shifted. The best agreement is obtained between 1350 to 1000 cm^{-1} (see Fig.2b), whereas a shift is required to bring the theory band positions into agreement with experiment between 1600 and 1300 cm^{-1} (see Fig.2a) and between 1000 and 600 cm^{-1} (see Figs.2b and 2c) as reported in previous work (An et al. 2016). Except for a peak around 700 cm^{-1}, that is not predicted by present theory, however was observed previously in experiments by (An et al. 2016) (band at 668 cm^{-1}). The present theory indicates a very weak band at 656 cm^{-1}.

An et al. (2016) have obtained experimental and theoretical FTIR spectra of terpenoids, namely isoprene, α-pinene, and β-pinene. These substances have fingerprint spectra that make possible to distinguish them from unidentified mixtures. The results of this combined experimental and theoretical show that the experimental spectra can be predicted using first-principles calculations, with some minor variations allowed by molecular stacking interactions and the local environment, which affect the degree of freedom of molecules (including translational, rotational, and vibrational).

Fig. 1 presents the non-irradiated band positions of α-pinene while Figures 2 a-c show the computed and measured mid-infrared spectra of α-pinene. Table 1 presents the theoretical and experiment IR values obtained in this work and in previous work An et al. (2016).

Comparing the current non-irradiated results with the ones obtained from An et al. (2016), most of them are in very good agreement. The fingerprint spectrum of this molecule (see Fig. 2) shows a weak peak at 703.7 cm^{-1} and a very strong peak at 787.5 cm^{-1} (CH bend), which

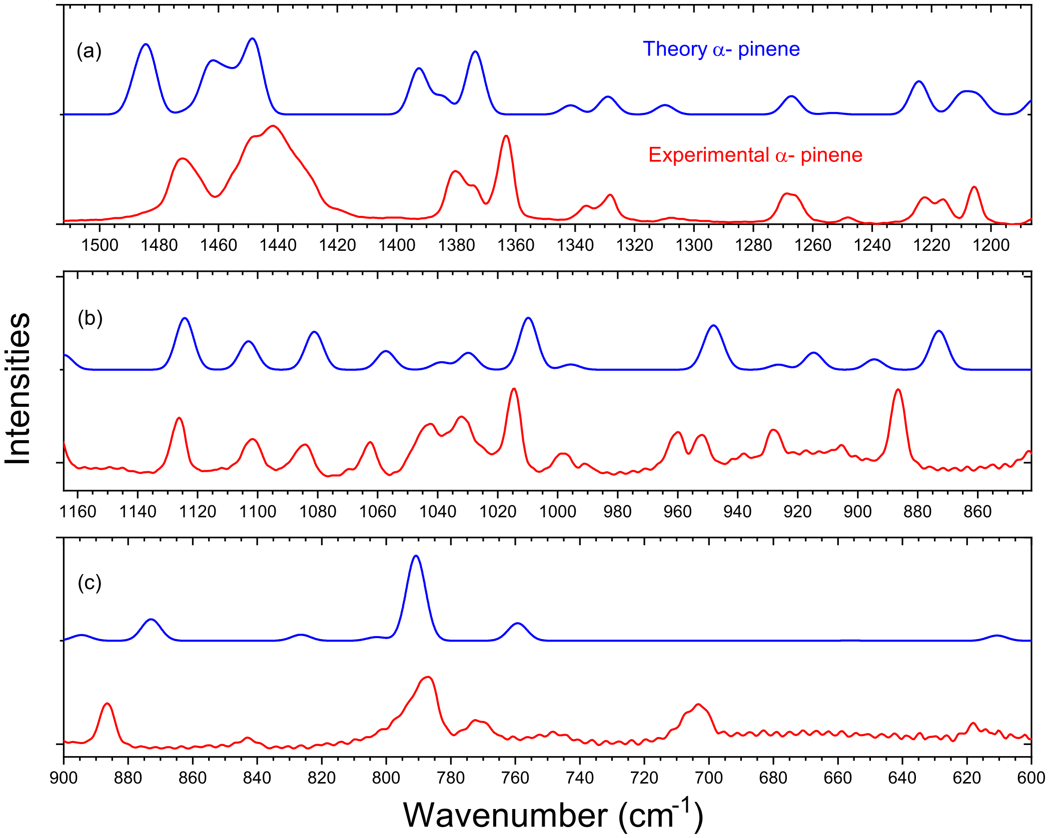

Figure 2. Comparison of the computed mid-infrared spectrum (shown in blue) with the laboratory normalized mid-infrared spectrum (shown in red) for non-irradiated neutral α-pinene at 10 K. (a) from 1550 to 1200 cm^{-1}; (b) from 1150 to 850 cm^{-1} and (c) from 900 to 600 cm^{-1}.

bears a shoulder at 770.0 cm^{-1} (ring deformation) and shows agreement with the estimated 790.8 cm^{-1} mode. The same strong peak appears at 770.0 cm^{-1} of An et al. (2016), followed by a medium peak at 668.0 cm^{-1} and a very small peak at 788.0 cm^{-1}.

Furthermore, it is possible to identify α-pinene by using a few rather strong peaks, such as 884.4 cm^{-1}, 951.3 cm^{-1}, 1014.2 cm^{-1}, 1125.9 cm^{-1}, 1205.1 cm^{-1}, 1217.6 cm^{-1}, 1268.3 cm^{-1}, and 1337.9 cm^{-1}, as representative IR-active modes. Assuming the predicted single molecule IR intensities as references (Qiu et al. 2010; An et al. 2016), the development of a few couples of teeth peaks (1083.8/1101.1 cm^{-1}, 1205.5 cm^{-1}, 1441.5 cm^{-1}, 1471.5 cm^{-1}, etc.) with broadening halfwidth and small red shifts are attributed to molecular stacking and inter molecular interactions.

A set of peaks that fall between 1040 and 1124 cm^{-1} shows a one-to-one correspondence with the computed infrared spectra, which is attributed to CH$_2$ twisting and CH bend. Similar band agreements can be obtained in the low-frequency regions, which Table 1 lists as 400–770 cm^{-1} (ring deformation) and 840–960 cm^{-1} (C skeleton deformation; CH bend).

The knowledge of the A-values is required to obtain the column densities, N(F), from both astronomical and laboratory spectra, and allows one to obtain the molecule abundances in the outer solar system and in the ISM. The Lambert-Beer equation was used to convert integrated absorbance, $S(F)$, into column densities, N(F), for all fluences, F (de Barros et al. 2016).

4.2 Integrated band strengths

The experimental integrated band strengths, A_i^{exp} (cm molecule^{-1}), of all the bands, except the C-H stretching modes, where obtained by equation (2): the experimental band integrated absorbance is divided by the number of molecules N(F). This quantity is computed as the sum of all the experimentally measured PAH band areas divided by the total theoretically calculated absolute intensities in the 1600-1000 cm^{-1} range (see for example (de Barros et al. 2017).

$$A_i^{exp} = \frac{\int_{\upsilon_{i,1}}^{\upsilon_{i,2}} \tau_{i,\upsilon} d\upsilon}{N(F)} = 2.303 \frac{\int_{\upsilon_{i,1}}^{\upsilon_{i,2}} A_{i,\upsilon} d\upsilon}{N(F)} = \sum_{j=0}^{M} A_j^{\alpha} \frac{\int_{\upsilon_{i,1}}^{\upsilon_{i,2}} \tau_{i,\upsilon} d\upsilon}{\sum_{i=0}^{L} \int_{\upsilon_{i,1}}^{\upsilon_{i,2}} \tau_{i,\upsilon} d\upsilon} \tag{2}$$

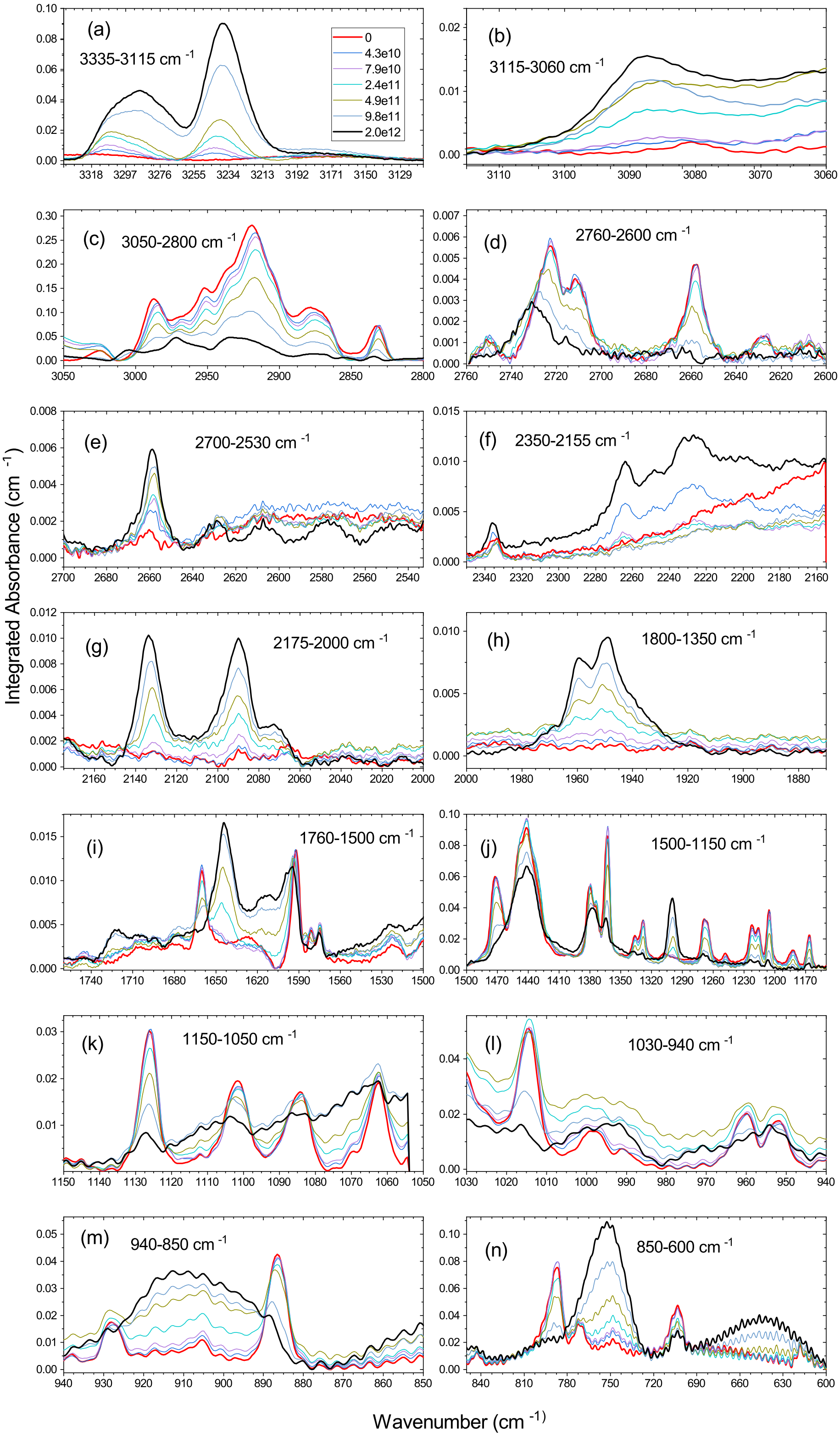

Figure 3. Mid-IR spectra of the non-irradiated and irradiated α-pinene ice for fluences ranging from 0 - 2 × 10^{12} ions cm^{-2}. Spectral regions: (a) 3335 to 3115 cm^{-1}, (b) 3115 to 3060 cm^{-1}, (c) 3050 to 2800 cm^{-1}, (d) 2760 to 2600 cm^{-1}, (e) 2700 to 2530 cm^{-1}, (f) 2350 to 2155 cm^{-1}, (g) 2175 to 2000 cm^{-1}, (h)1800 to 1350 cm^{-1}, (i) 1760 to 1500 cm^{-1}, (j) 1500 to 1150 cm^{-1}, (k) 1150 to 1050 cm^{-1}, (l) 1030 to 940 cm^{-1}, (m) 940 to 850 cm^{-1}, and (n) 850 to 600 cm^{-1}.

Table 1. Summary of neutral α-pinene band positions in the MIR (600 to 1800 cm^{-1}) region (in cm^{-1} and μm), A-values (km mol^{-1}), theoretical band positions (cm^{-1}), absolute intensities (km mol $^{-1}$), and band assignments.

Wavenumber (cm^{-1})	Wavelength (μm)	Integrated region (cm^{-1})	A value[a] (km mol $^{-1}$)	Theoretical Position (cm^{-1})	Theoretical Abs. Intensity (km mol $^{-1}$)	Experimental[b] Infrared (cm^{-1})	Calculated[b] Position (cm^{-1})	Assignment/ Comments
This	work					Previous	work	
703.7	14.3	713.9 - 696.6	2.26	656.2	0.047	668 (m.)	658 (w.)	Ring deformation
747.8	13.4	779.1 - 762.7	2.76	759.3	2.535	-	-	Ring deformation
770.0	12.9	807.5 - 779.1	2,77	769.4	0.011	770 (s.)	761 (m.)	Ring deformation
787.5	12.7	806.6 - 801.7	12.26	790.8	12.3	788 (vs.)	789 (vs.)	CH bend
842.1	11.9	854.8 - 836.5	1.18	845.3	1.640	840 (m.)	829 (w.)	C skeleton deformation; CH bend
884.4	11.3	894.8 - 878.4	4.87	880.1	0.025	883(s.)	877 (m.)	C skeleton deformation; CH bend
904.4	10.8	911.2 - 902.5	0.45	894.5	0.829	903 (w.)	898 (w.)	C skeleton deformation
927.5	10.8	935.3 - 923.2	1.35	926.4	0.402	927 (m.)	919 (w.)	C skeleton deformation; CH_3asymmetric deformation
951.7	10.5	656.5 - 944.5	1.26	949.4	1.875	953 (s.)	952 (m.)	C skeleton deformation; CH_2 twisting; CH_3 asymmetric deformation
960.3	10.4	968.6 - 956.0	1.61	995.7	0.413	997 (w.)	998 (w.)	CH_3 asymmetric deformation
998.1	10.0	1010.9 - 1011.6	0.16	997.8	0.230	989(w.)	986 (w.)	CH_3 asymmetric deformation
1014.2	9.86	1022.1 - 1006.6	4.43	1009.8	0.370	1013 (s.)	1012 (m.)	CH_3 asymmetric deformation; CH bend; CH_2 twisting
1032.8	9.68	1038.9 - 1022.5	2.01	1032.7	0.181	-	1034(w.)	CH_2 twisting; CH bend
1041.9	9.59	1052.9 - 1038.5	1.96	1041.8	4.157	1040 (w.)	1034 (w.)	CH_2 twisting; CH bend
1061.9	9.42	1068.8 - 1056.3	2.16	1057.3	1.491	1061 (m.)	1059 (w.)	CH_2 twisting; CH bend
1083.8	9.18	1093.4 - 1077.0	2.37	1081.1	3.040	1085 (m.)	1082 (m.)	CH_2 twisting; CH bend
1101.0	9.07	1110.3 - 1093.9	2.41	1103.1	2.275	1100 (m.)	1099 (m.)	CH bend; CH_2 twisting
1144.8	8.73	1148.9 - 1138.0	0.23	1140.7	1.141	1143 (w.)	1143 (w.)	CH bend
1125.9	8.88	1134.9 - 1118.0	3.53	1124.3	4.141	1124 (s.)	1123 (m.)	CH bend
1166.5	8.57	1172.9 - 1159.9	2.12	1164.6	1.175	1167 (m.)	1163 (w.)	CH bend; C–C_5C bend; CH_2 twisting
1182.8	8.46	1190.8 - 1175.9	1.33	1185.1	2.139	1183 (m.)	1181 (w.)	C–C–C bend; CH bend; CH_3 asymmetric deformation
1205.5	8.29	1210.6 - 1198.5	2.95	1204.5	2.390	1204 (s.)	1203 (m.)	CH_2 wagging; CH_2 twisting; CH_3 asymmetric deformation
1215.5	8.22	1215.9 - 1210.1	1.53	1210.2	2.568	1218 (s.)	1220 (s.)	CH_2 wagging; CH bend; CH_2 twisting
1222.4	8.18	1230.3 - 1222.6	2.56	1224.3	4.511			
1248.7	8.01	1254.9 - 1242.4	0.53	1249.0	0.110	1249 (m.)	1248 (w.)	CH bend
1268.3	7.87	1280.9 - 1254.9	5.01	1267.2	2.494	1265 (s.)	1265 (m.)	CH bend; CH_2 twisting
1307.3	7.64	1314.2 - 1297.4	0.51	1309.7	1.274	1308 (w.)	1307(w.)	CH bend; CH_2 wagging
1327.4	7.54	1333.5 - 1322.4	1.57	1328.9	1.572	1331 (s.)	1325 (m.)	C–C stretching; CH bend; CH_2 wagging
1337.9	7.48	1341.7 - 1333.0	0.44	1341.5	1.245		1328 (m.)	CH_2 wagging; CH bend
1363.0	7.34	1370.1 - 1354.7	7.94	1367.1	0.140	1367 (vs.)	1373 (vs.)	CH_3 symmetric deformation
1373.9	7.28	1385.6 - 1370.1	1.77	1373.6	8.560	1377 (m.)	1378 (m.)	CH_3 symmetric deformation
1381.1	7.25	1389.4 - 1370.1	5.08	1384.7	2.384	1380 (vs.)	1391 (vs.)	CH3 symmetric deformation
1431.7	6.98	1460.8 - 1409.7	4.02	1392.6	6.212	1437 (vs.)	1439 (vs.)	CH_2 scissoring
1441.5	6.93	1460.8 - 1409.7	4.01	1447.7	7.182	1443 (vs.)	1449 (vs.)	CH_2 scissoring
1449.2	6.90	1504.2 - 1463.2	15.0	1449.6	3.032	1459 (vs.)	1448 (vs.)	CH_3 asymmetric deformation
1471.5	6.79	1481.9 - 1460.8	11.3	1463.3	0.832	1469 (vs.)	1469 (vs.)	CH_2 scissoring; CH_3 asymmetric deformation
1573.2	6.36	1577.9 - 1570.2	0.20	1483.4	7.482	1570 (w.)		
1581.2	6.32	1585.6 - 1577.9	0.39					
1593.4	6.28	1605.9 - 1585.6	1.66	-	-			
1627.6	6.14	1647.8 - 1607.3	1.67					
1661.2	6.02	1669.5 - 1647.8	1.42	1680.4	1.562	1659 (w.)	1660 (vs.)	C_5C stretching

Note: (vs.)—very strong, (s.)—strong, (m.)—medium, (w.)—weak. [a]A-values $\geq$ 2 km mol $^{-1}$ are given.[b]Experiments at room temperature (An et al. 2016).

where $\tau_{i,\nu}$ is the optical depth of mode i at frequency υ (cm^{-1}), $A_{i,\nu}$ is the absorption coefficient of mode i at frequency υ (cm^{-1}), A_j^{α} is the theoretically calculated absolute intensity of vibrational mode j in the 1600 to 1000 cm^{-1} range, in cm $molecule^{-1}$, M is the number of theoretically calculated modes in the respective region, L is the number of measured modes, and $\upsilon_{i,1}$ and $\upsilon_{i,2}$ are the lower and upper integration boundaries in cm^{-1}, respectively, for absorption feature i.

Using the experimental A-values A_i^{exp} listed in Table 1, the column density N(F) can be obtained via the equation (3):

$$N(F) = ln10 \frac{\int_{\upsilon_{i,1}}^{\upsilon_{i,2}} \tau_{i,\upsilon} d\upsilon}{A_i^{exp}} \tag{3}$$

The column densities of the five most intense bands of α-pinene namely 1268.3, 1205.1, 1125.0, 1014.2 and 787.5 cm^{-1}, were determined, using the A-values reported in Table 1. Fig. 5a shows that the calculated column densities for the five bands strengths are in excellent agreement $N_0 \sim 4.2 \times 10^{18}$ $molecules.cm^{-2}$. Based on this agreement, the 787.5 cm^{-1} band of α-pinene was selected to compute the cross sections reported in Table 3.

4.3 Radiolysis of $\alpha-$pinene: product formation

The comparison between the non-irradiated and the irradiated at a fluence of 2×10^{12} $molecules.cm^{-2}$ is shown in Fig.4. We did not observed evident signs of racemization(Cataldo et al. 2007a; Cataldo 2007b).

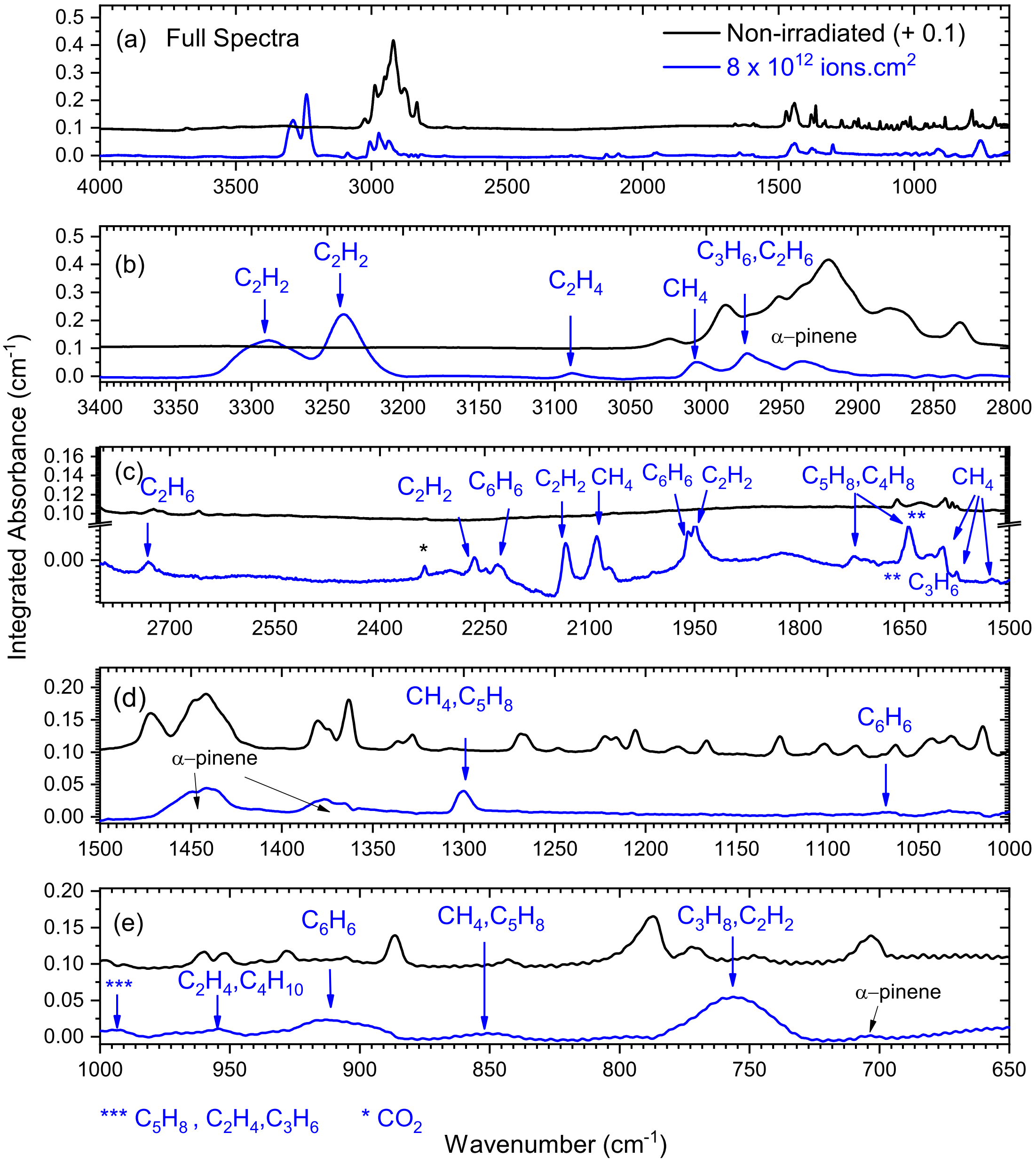

Figure 4. Comparison of the non-irradiated (in black) mid-infrared spectrum and irradiated α-pinene for a fluence of 8×10^{12} ions.cm^{-2} (shown in blue) at 10 K. (a) full spectra from 4000 to 650 cm^{-1} wavenumbers; (b) from 3400 to 2800 cm^{-1}; (c) from 2750 to 1500 cm^{-1}; (d) from 1500 to 1000 cm^{-1} and (e) from 1000 to 650 cm^{-1}.

In general, ony realatively small molecular species can be unambiguously identified by FTIR, such as methane that has been found to be a component of ISM ices. For large molecules, the identification is given through the functional groups (Boogert et al. 2015). As the number of molecular species during irradiation increases (Fig. 3, some of the infrared vibrations start to overlap. In Table 2 several bands can be identified as belonging to more than one molecular species. This clearly illustrates how the hydrocarbons larger than C_2H_m start to have extensive overlap of their most intense vibration bands, making identification very challenging. Cataldo (2007c) irradiated α-pinene using γ radiation and a 600 kGy radiation dose, producing samples of ocimene and dipentene together with minor quantities of other products and a resin.

In the current experiment more than ten different products were formed. The difference in the chemical processes that occur after γ and ion-beam irradiation reflect these differences in spatial energy deposition. γ irradiation results in sparse ionization, largely in spurs, with an average of one or two ionization's per spurs that are formed by the cascade of electrons that results from the initial photon interactions with

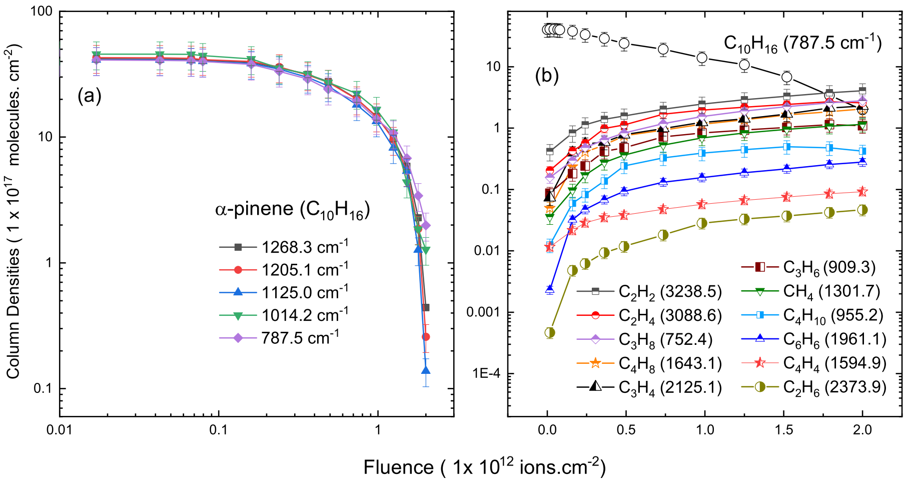

Figure 5. Dependence of column densities on fluence: (a) for the five stronger bands of α-pinene, and (b) for the 787.5 cm^{-1} band of α-pinene and for the eleventh products formed during irradiation. Solid lines are given guides to the eye.

target molecules (Turner et al. 1983). With an ion-beam, however, energy is deposited by the projectile along its track by relatively frequent interactions of the ion with target molecules, resulting in a concentrated deposition of energy along the ion path (Muroya et al. 2006; Adhikary et al. 2014).

In 61.3 MeV $^{84}Kr^{15+}$ ion bombardment experiment, twelve hydrocarbons were formed: methane (CH_4), acetylene (C_2H_2), ethylene (C_2H_4), propylene (C_3H_6), propane (C_3H_8), n-butane (C_4H_{10}), butene (C_4H_8), propyne (C_3H_4), benzene (C_6H_6), ethane (C_2H_6), vinylacetylene (C_4H_4) and 2-methyl-1,3-butadiene or isoprene (C_5H_8). Detailed spectra of all the new bands formed during the irradiation are shown in Fig. 3. Fourteen spectrum sets display the evolution of the pure α-pinene made during the irradiation of $^{84}Kr^{15+}$ ion beam up to the final fluence of 2.0×10^{12} ions.cm^{-2}. Tables 2 and 3 list the molecular bands observed during irradiation of α-pinene, their wavelengths, absorption modes, and literature A-values. Following this order and explaining each product in detail, there are:

(1) eight methane bands were monitored, namely three fundamental vibrations at 1301.7 (ν_7), 1522.2 (ν_2) and 3007.5 cm^{-1} (ν_7) (Mejía et al. 2013; Bernstein et al. 2005; Bouilloud et al. 2015; Bennett et al. 2006) and at bands identified by Kaiser & Roessler (1998) at 2088.5 cm^{-1}, some ring vibrations bands in the 1600 - 1580 cm^{-1} region, as 1609.1, 1594.9 and 1578.5 cm^{-1} and another weak band at 851.8 cm^{-1}. Some very weak fundamental bands appear in the region 2650 - 2550 cm^{-1}, those may correspond to the $2\nu_4$ vibrations, also observed by Kaiser & Roessler (1998), for details see Fig.3e and Tables 2 and 3. The fundamental band at 1301.7 cm^{-1} was used for the cross section calculation as shown in Fig.5b with A-value of 5.0×10^{-18} cm.molecule^{-1} (Mejía et al. 2013).

(2) four acetylene fundamentals identified at about 752.4 (ν_5), 2242.0 (ν_3), 2191.1 (ν_1) and 3238.5 cm^{-1} (ν_3) in good agreement with Lee et al. (2007); Kim et al. (2010); Mejía et al. (2013); Hudson et al. (2021) experiments. The band at 638.2 cm^{-1} is very broad and was observed by Kaiser & Roessler (1998); Hudson et al. (2014b), details in Fig.3n. A combination band was observed at 3291.6 ($\nu_2 + \nu_4 + \nu_5$) Lee et al. (2007); Kim et al. (2010). For the cross sections calculations, we use the fundamental band 3238.5 cm^{-1} with with A-value of 5.0×10^{-18} cm.molecule^{-1} (Mejía et al. 2013; Bernstein et al. 2005; Bouilloud et al. 2015).

(3) two ethylene fundamentals identified at about 955.2 (ν_7) and 3088.6 cm^{-1} (ν_9) in full accord with literature values (Kim et al. 2010; Bernstein et al. 2005; Bennett et al. 2006). Note that ν_7 of ethylene appeared quite blend with a group of absorption's near the 950 cm^{-1} region. The band's A-values, 15 and 1.7×10^{-18} cm.molecule^{-1} (Mejía et al. 2013; Bernstein et al. 2005; Kim et al. 2010; Bennett et al. 2006) were extracted from the literature.

(4) four propylene bands identified as CH bend at 993.5 cm^{-1}, a CH_2 bend/cc stretch at 909.3 cm^{-1}, C≡C stretch at 1643.1 cm^{-1} and a CH_2 s-stretch at 2973.9 cm^{-1}. The last one was used for the column densities calculation with A-values of 10.7×10^{-18} cm.molecule^{-1} (Hudson et al. 2021).

(5) a fundamental band of propane observed at 752.4 cm^{-1} used for the column densities calculation with A-values of 0.8×10^{-18} cm.molecule^{-1} (Mejía et al. 2013; Hudson et al. 2021).

(6) four additional fundamental band identified for n-butane at 955.2 (ν_{16}), 946.6 (ν_{16}), 2874.7 (ν_{28}) and 2932.1 (ν_{13}), all identified by Kim et al. (2010). The 955.2 (ν_{16}) band with A-value of 1.8×10^{-18} cm.molecule^{-1} was used for the cross sections calculations (Kim et al. 2010).

(7) three bands of butene observed in this experiment, a C≡C str. at 1643.1 cm^{-1}, a HC=CH wag vibration mode at 995.5 cm^{-1} and a vibration mode = CH_2 wag at 909.3 cm^{-1}. The 1643.1 cm^{-1} band was choosen for the column density calculation, using the A-value of 1.3 $\times 10^{-18}$ cm.molecule^{-1} (Kim et al. 2010). That band at 1643.1 cm^{-1} (C≡C str.) can be also related to isoprene molecule (C_5H_8) An et al. (2016).

Table 2. Molecular bands observed in the current work during irradiation of α-pinene in region from 3291.6 to 2088.5 cm^{-1}. Wavelengths; absorption modes, A-values.

Position α-pinene (cm^{-1})	Literature values (cm^{-1})	Identified molecules	Absorption mode	A-values $\times 10^{-18}$ cm molecule^{-1}
3291.6	3294.8	C_2H_2 (acetylene) [a]	ν_2 + ν_4+ ν_5	-
3238.5	3240	C_2H_2 (acetylene)[b,c]	ν_3	**12[b]**
3088.6	3090	C_2H_4 (ethylene)[c,d,e,f]	ν_9	**1.7[d], 1.5[c,f]**
	3088	C_6H_6 (benzene)[g,h]	ν_1 + ν_6+ ν_8	**11[g]**
3007.5	3009	CH_4 (methane)[b,e,i]	ν_3	**10.5[b]**
2973.9	2974	C_2H_4 (ethylene)[m]	CH_2 s-str.	-
	2975	C_2H_6 (ethane)[b,d,f]	ν_{10}	**14.8[b], 20[f]**
	2977	C_3H_6 (propylene)[j]	CH_2 s-str.	**10.7[j]**
	2973	C_4H_4 (vinylacetylene)[k,l]	ν_6+ν_7	-
2932.1	2930	C_4H_{10} (n-butane)[d]	ν_{13}	-
2874.7	2872	C_4H_{10} (n-butane)[d]	ν_{28}	-
	2872	C_3H_8 (ethane)[j]	-	-
	2880	C_2H_6 (ethane)[f]	-	**3.51[f]**
2734.6	2736	C_2H_6 (ethane)[b,d]	ν_2 + ν_6	**0.2[b]**
2645.4	2642	CH_4 (methane)[m]	2ν_4	-
2619.1	2614.3	CH_4 (methane)[m]	2ν_4	-
2602.1	2599.1	CH_4 (methane)[m]	2ν_4	-
2578.3	2591.1	CH_4 (methane)[m]	2ν_4	-
2545.0	-	CH_4 (methane)	2ν_4	-
2260.5	2257	C_2H_2 (acetylene)[a]	-	
	2257	R-C ≡ CR'	C≡C	-
		(R,R'-disubstituted acetylene) [m]		-
2242.0	2242	C_2H_2 (acetylene)[a,c]	ν_3	-
	2242	R-C ≡ CR'	C≡C	-
		(R,R'-disubstituted acetylene) [m]		-
2228.3	2227	C_2H_4 (ethylene)[m]	C≡C	-
	2227	R-C ≡ CR'	C≡C	-
		(R,R'-disubstituted acetylene) [m]		-
2191.1	2193	R-C ≡ CR'	C≡C	-
		(R,R'-disubstituted acetylene) [m]		-
	2193	C_2H_2 (acetylene)[c]	ν_1	-
2172.7	2167	C_2H_4 (ethylene)[m]	C≡C	-
	2170	R-C ≡ CR'	C≡C	-
		(R,R'-disubstituted acetylene) [m]		-
2134.6	2136	H-C ≡ C-R	C≡C	-
		(monosubstituted acetylene)[m]		-
2125.1	2124	C_3H_4 (propyne)[j]	C≡C stretch	**0.47[j]**
2088.5	2087	CH_4 (methane)[m]	C≡C	-
	2087	H-C ≡ C-R	C≡C	-
		(monosubstituted acetylene)[m]		-

[a] Lee et al. (2007); [b] Mejía et al. (2013); [c] Abplanalp & Kaiser (2020); [d] Kim et al. (2010); [e] Bennett et al. (2006); [f] Hudson et al. (2014a), [g] Ruiterkamp et al. (2005) [h] Strazzulla & Baratta (1991); [i] Bouilloud et al. (2015); [j] Hudson et al. (2021); [k] Zhou et al. (2010); [l] Kim & Kaiser (2009). [m] Kaiser & Roessler (1998); [n] An et al. (2016).

(8) only one band of propyne observed at 2125.1 cm^{-1} C≡C stretch Hudson et al. (2021), for the column density calculation, the A-value of 0.47 × 10^{-18} cm.molecule^{-1} has been used (Hudson et al. 2021).

(9) three benzene bands observed, two fundamental bands at 3088.6 cm^{-1} (ν_{10}) and 1037.5 cm^{-1} (ν_{18}), and one combination band at 1961.1 (ν_{17} + ν_5) (Ruiterkamp et al. 2005; Strazzulla & Baratta 1991). The fundamental band 1037.5 cm^{-1} with the A-value of 2.5 × 10^{-18} cm.molecule^{-1} was use for the column density and cross section calculations.

(10) two ethane bands identified, a fundamental 2973.9 cm^{-1} (ν_{10}) and a combination band at 2734.6 cm^{-1} (ν_2 + ν_6) (Kim et al. 2010; de Barros et al. 2016). The band 2730.6 cm^{-1} was used to determine the column densities with the A-value of 0.2 × 10^{-18} cm.molecule^{-1} (de Barros et al. 2016).

(11) six possible bands of C_4H_4 were observed in our experiment. The vinylacetylene is thermodynamically less stable than the methylenecyclopropene isomer of vinylacetylene, the molecule was visible through its ν_6+ν_7, ν_9+ν_{10}, ν_1, ν_6, ν_{15} and ν_2 carriers at 2973.9, 1949.7, 1750.2, 1594.9, 946.5 and 646.2 cm^{-1} respectively. (Zhou et al. 2010) and co-workers confirmed this band in irradiated $^{13}C_2H_2$ ices through its absorptions at 1711 and 648 cm^{-1} attributed to the ν_{14} and ν_3 bands, respectively.

(12) three 2-methyl-1,3-butadiene or isoprene molecule were identified: 1643.1, 1301.7 and 955.2 cm^{-1} (ν_{10}) as C=C str., CH bend and

Table 3. Molecular bands observed in the current work during irradiation of α-pinene in region 1961.1 to 642.2 cm^{-1}. Wavelengths; absorption modes, A-values.

Position α-pinene (cm^{-1})	Literature values (cm^{-1})	Identified molecules	Absorption mode	A-values $\times 10^{-18}$ cm $molecule^{-1}$
1961.1	1960	C_6H_6 (benzene)[g]	$\nu_{17} + \nu_5$	-
	1961	C_2H_2 (acetylene)[c]	ν_2	-
1949.7	1951	RCH=C=CH_2[c,m]	C≡C≡C	-
	1951	C_4H_4 (vinylacetylene)[k,l]	$\nu_9 + \nu_{10}$	-
1750.2	1762	C_4H_4 (methylenecyclopropene) [j,k]	ν_1	**3.2**[j]
1643.1	1643	C_4H_8 (butene)[d]	C=C str.	**1.3**[d]
	1644	C_3H_6 (propylene)[j]	C=C str.	**1.69**[j]
	1643	C_5H_8 (2-Methyl-1,3-butadiene or isoprene)[n]	C=C str.	-
1609.1	1607	Mono, o, m, p, 1.2.4-, 1,3,5-substituted benzene[m]	ring vibrations	-
1594.9	1596.1	CH_4 (methane)[m]	ν_4	-
	1599	C_4H_4 (vinylacetylene)[k,l]	ν_6	**1.4**[l]
	1598	C_5H_8 (2-Methyl-1,3-butadiene or isoprene)[n]	CH bend	-
1578.5	1581	Mono, o, m, p, 1.2.4-, 1,3,5-substituted benzene[m]	ring vibrations	-
	1582	CH_4 (methane)[b]	ring vibrations	-
1522.2	1523	CH_4 (methane)[e]	ν_2	-
1301.7	1304	CH_4 (methane)[b,i,n,m]	ν_4	**7.76**[b]
	1303	C_5H_8 (2-Methyl-1,3-butadiene or isoprene)[n]	CH bend	-
1037.5	1038	C_6H_6 (benzene)[g]	ν_{18}	**2.5**[g]
993.5	993	C_3H_6 (propylene)[j]	CH bend	**2.4**[j]
	993	C_4H_8 (butene)[d]	HC=CH wag	-
	993	C_5H_8 (2-Methyl-1,3-butadiene or isoprene)[n]	CH bend/CH_2wag. /CH_2twis.	-
955.2	952	C_2H_4 (ethylene)[b,d,e]	ν_7, CH_2wag.	**15**[b]
	960	C_4H_{10} (n-butane)[d]	ν_{16}	**1.8**[d]
	953	C_5H_8 (2-Methyl-1,3-butadiene or isoprene)[n]	CH_2wag./CH_2twis.	-
946.5	948	C_4H_{10} (n-butane)[d]	ν_{16}, CH_2wag.	**15**[d]
	944	C_4H_4 (vinylacetylene)[l]	ν_{15}	-
	949	C_2H_4 (ethylene)[d,f]	ν_{15}	**12.6**[f]
909.3	909	C_3H_6 (propylene)[j]	CH_2 bend/cc stret.	**8.33**[j]
	910	C_4H_8 (butene)[d]	= CH_2 wag	**6.0**[d]
851.8	855	Mono, o, m, p, 1.2.4-, 1,3,5-substituted benzene[m]	ring vibrations 2 free H	-
752.4	750	C_3H_8 (propane)[b,j]	ν_5	**0.8**[j]
	754	C_6H_6 (benzene)[f]	CH out of plane bend	-
	742	C_2H_2 (acetylene)[a,c,d]	ν_5	**30**[c]
	760	C_5H_8 (2-Methyl-1,3-butadiene or isoprene)[n]	CH_2 twisting	-
646.2	648	C_4H_4 (vinylacetylene)[j,k,l]	ν_2	-
	645	C_3H_4 (propyne)[j]	ν_2	**13.3**[j]

[a] Lee et al. (2007); [b] Mejía et al. (2013); [c] Abplanalp & Kaiser (2020); [d] Kim et al. (2010); [e] Bennett et al. (2006); [f] Hudson et al. (2014a), [g] Ruiterkamp et al. (2005) [h] Strazzulla & Baratta (1991); [i] Bouilloud et al. (2015); [j] Hudson et al. (2021); [k] Zhou et al. (2010); [l] Kim & Kaiser (2009). [m] Kaiser & Roessler (1998); [n] An et al. (2016).

CH_2 wag./CH_2 twister, respectively (An et al. 2016). Chen et al. (2013) also analyzed by FTIR, in details, the structure of some different polyisoprenes, C_5H_8 molecule.

Finally, the thermodynamically less stable ethylenecyclopropene isomer of vinylacetylene (C_4H_4) was visible through its ν_1 and ν_2 carriers at 1764 and 650 cm^{-1} respectively. (Zhou et al. 2010) confirmed this band by irradiating $^{13}C_2H_2$ ices through its absorption's at 1711 and 648 cm^{-1} attributed to the ν_{14} and ν_3 bands, respectively. All the A-values used for the column density calculations are listed at Tables 2 and 3. It can be seen in the amorphous α-pinene spectra, shown in Figs. 3f and 4, a very small peak that can be assign to CO_2 (2339.5 cm^{-1}) which is formed during irradiation via reactivity of α-pinene with small amount of water deposition. Hudson et al. (2021) also observed the same effect during their experiment irradiation.

4.4 $\alpha-$pinene destruction cross sections

4.4.1 Theory review

Whenever a molecular sample is exposed to an ion beam, the number of molecules of the original target (precursor) changes basically by two processes: radiolysis and sputtering. For thin targets, the radiolysis destruction cross section, σ_d, is constant along the projectile track, and the column density rate is given by (e. g. Duarte et al. (2009, 2010)):

$$\frac{dN}{dF} = -\sigma_d N - Y(F) \tag{4}$$

where N is the precursor column density and Y(F) is the sputtering yield, which in general varies when the beam fluence increases. For thick targets, the projectile energy decreases inside the material, requiring a more complex model (da Silveira 2022).

To solve Eq. 4 and get the destruction cross section, the Y(F) function must be known. Four realistic cases should be considered: (i) Y(F) = 0 means no sputtering, a situation that occurs inside the bulk; then, N(F) = N_0 exp $(-\sigma_d F)$. (ii) Y(F) = Y_0 is adequate for targets having volatile products, so that the precursor concentration in the surface remains constant during the irradiation (Duarte et al. 2010). (iii) Y(F) = Y_0/N_0 N(F) has been used for materials where the ion beam decreases the precursor concentration on its surface. As a consequence, N(F) = N_0 exp $(-\sigma_d^{ap} F)$, where σ_d^{ap} = σ_d + Y_0/N_0 is the so called apparent destruction cross section (Andrade et al. 2013). However, it turns out that the Y_0/N_0 coefficient is slightly underestimated, yielding good predictions only for short irradiations. For long ones, the small discrepancies are accumulative, and the model predicts that the precursor concentration decreases too slowly, and the sample cannot be completely destroyed. Finally, (iv) Y(F) = Y_0 exp $(-\sigma_d F)$.

For the ice analyzed in the current experiment, the best Y(F) function is Y(F) = Y_0 exp $(-\sigma_d F)$: it considers that the sample is homogeneously degraded by radiolysis and, at fluence F, when an internal layer starts to suffer sputtering, the precursor concentration has been decreased by exp $(-\sigma_d F)$. The solution of Eq. 4 is then (Mejía et al. 2020):

$$N(F) = (N_0 - Y_0 F)\exp(-\sigma_d F) \tag{5}$$

Interestingly, this equation predicts that, for any σ_d, all the precursor molecules are removed or destroyed at F_{max} = Y_0/N_0. Therefore, N(F_{max}) = 0 is a practical method to directely determine the sputtering yield, Y_0, without the influence of the radiolysis.

4.4.2 Measuring the precursor destruction cross section and its sputtering yield

In the current article, the α-pinene column density was determined from absorbance evolution of the 787.5 cm^{-1} band. Its evolution is presented in Fig. 6 and is very well fitted by Eq.(5). For the 61.3 MeV $^{84}Kr^{15+}$ ion beam, the obtained radiolysis cross section is $\sigma_d = 5.4 \times 10^{-13}$ cm^2 and the initial sputtering yield is $Y_0 = 1.8 \times 10^6$ molec. per impact. Since $N_0 = 4.3 \times 10^{18}$ molecules cm^{-2}, the fluence predicted to eliminate all the α-pinene molecules from the sample is $F_{max} = N_0/Y_0 = 2.3 \times 10^{12}$ ions cm^{-2}. As shown in Fig. 6, this value agrees very well with the extrapolation of the sequence of data points. Note also that $\sigma_d^{ap} = \sigma_d + Y_0/N_0 = \sigma_d + 1/F_{max} = (5.4 + 4.3) \times 10^{-13}$ cm^2, which shows that the two processes are about equally destructive at the beginning of the irradiation.

4.5 Products: formation cross sections

The observed column density evolution of each product behaves according to the approximate expression used previously in similar analyses (Andrade et al. 2013).

$$\frac{N_k(F)}{N_0} \approx \sigma_{f,k}[F - \frac{1}{2}\sigma_{d,k}^{eff} F^2] \tag{6}$$

where $\sigma_{f,k}$ is the formation cross section, the relevant parameter in this analysis, and $\sigma_{d,k}^{eff} = \sigma_d + \sigma_{d,k}$ is the effective destruction cross section for a specific product; σ_d refers to the precursor destruction and $\sigma_{d,k}$ to the destruction of this product. This approximation requires $\sigma_{d,k}^{eff}$ F << 1, condition fulfilled, since $\sigma_{d,k}^{eff} \approx 5 \times 10^{-13}$ cm^2 and F runs in the × 10^{12} molecules cm^{-2} range. Sputtering is negligible for products at the outset of the experiment. The distinct destruction cross sections of product are responsible for the small variations observed in the N_k(F) shapes.

Eq. (6) shows that a N_k(F) plot, in log-log scale, is characterized by: (i) a linear shape at low fluence, with a unitary angular coefficient, and (ii) a light curvature occurring around F = × 10^{12} molecules cm^{-2}. This is exactly what is seen in Figs. 7b-l, for eleven product species produced by the radiolysis. The formation and destruction cross sections of product from the fittings and are presented in Table 4.

From Table 4 it is observed that C_3H_4 has the highest formation cross section (~ 4 × 10^{-14} cm^2), followed by C_2H_2, C_3H_6, C_4H_8 (~ 3 × 10^{-14} cm^2), C_4H_{10}, C_4H_4 and C_2H_6 (~ 2 × 10^{-14} cm^2), C_6H_6 (~ 1 × 10^{-14} cm^2), CH_4 and C_4H_4 (~ 0.5 × 10^{-14} cm^2). The molecular species C_3H_8 has the lowest cross section: ~ 0.3 × 10^{-14} cm^2.

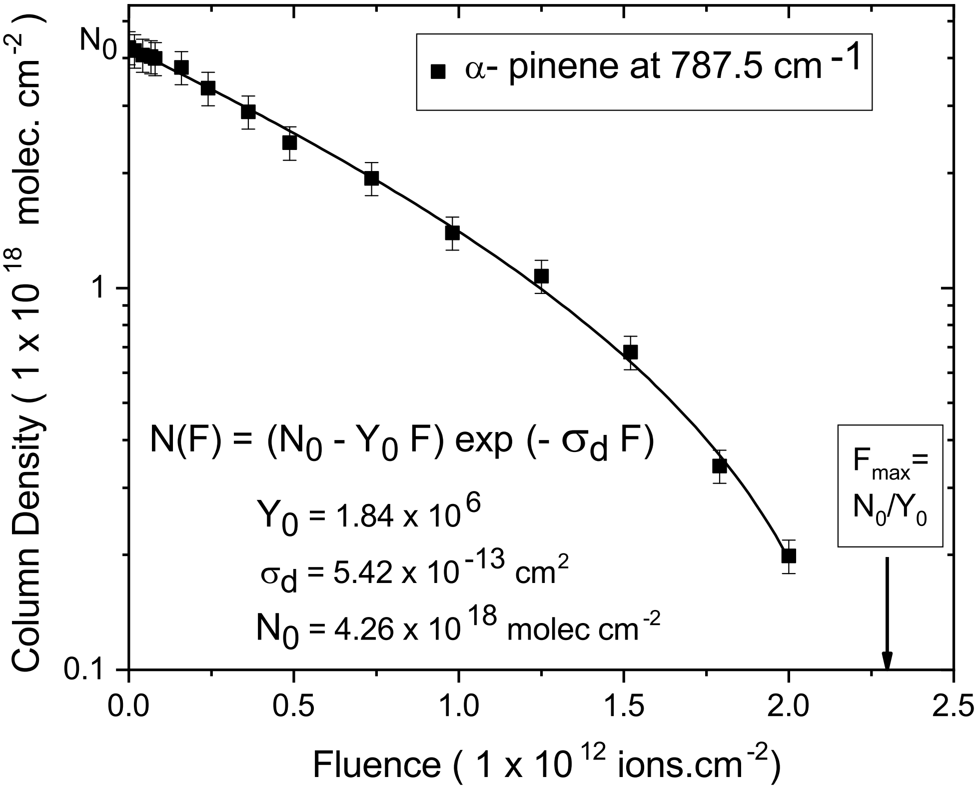

Figure 6. Column density evolution of α-pinene as a function of fluence for the band 787.5 cm^{-1}.

Table 4. Wavelengths, destruction (σ_d) cross sections of α-pinene and formation ($\sigma_{f,k}$) and destruction ($\sigma_{d,k}$) cross sections of products listed in Tables 2 and 3 and the initial and final column densities. Cross sections were obtained by fitting the product column density evolution with Eq. (6). The destruction (σ_d) G-values is defined as 100 σ/S_e (Duarte et al. 2010), where S_e = 5.8 × 10^2 eV /10^{15} molec.cm^{-2}.

Molecules	Frequency cm^{-1}	ΔN 10^{18} molec.cm^{-2}	σ_d 10^{-13} cm^2	G_d (molec/100 eV)
α-pinene	787.5	-4.1	5.42 ± 0.47	0.93

Molecules	Frequency cm^{-1}	ΔN 10^{17} molec.cm^{-2}	$\sigma_{f,k}$ 10^{-14} cm^2	$\sigma_{d,k}$ 10^{-14} cm^2
C_2H_2	3238.5	20	2.82 ± 0.83	0.22 ± 0.03
C_2H_4	3088.6	2.6	0.48 ± 0.09	0.35 ± 0.02
C_3H_8	752.4	2.7	0.27± 0.05	0.20 ± 0.09
C_4H_8	1643.1	2.1	3.08 ± 0.09	0.25 ± 0.05
C_3H_4	2125.1	2.3	3.88 ± 0.27	0.38 ± 0.06
C_3H_6	993.5	1.1	3.01 ± 0.16	0.18 ± 0.04
CH_4	1301.7	1.1	0.52 ± 0.07	0.12 ± 0.07
C_4H_{10}	955.2	0.4	2.05 ± 0.10	0.27 ± 0.06
C_6H_6	909.3	0.3	1.11 ± 0.08	0.24 ± 0.07
C_4H_4	1594.9	0.09	1.98 ± 0.53	0.18 ± 0.05
C_2H_6	2973.9	0.05	1.69 ± 0.78	0.25 ± 0.09

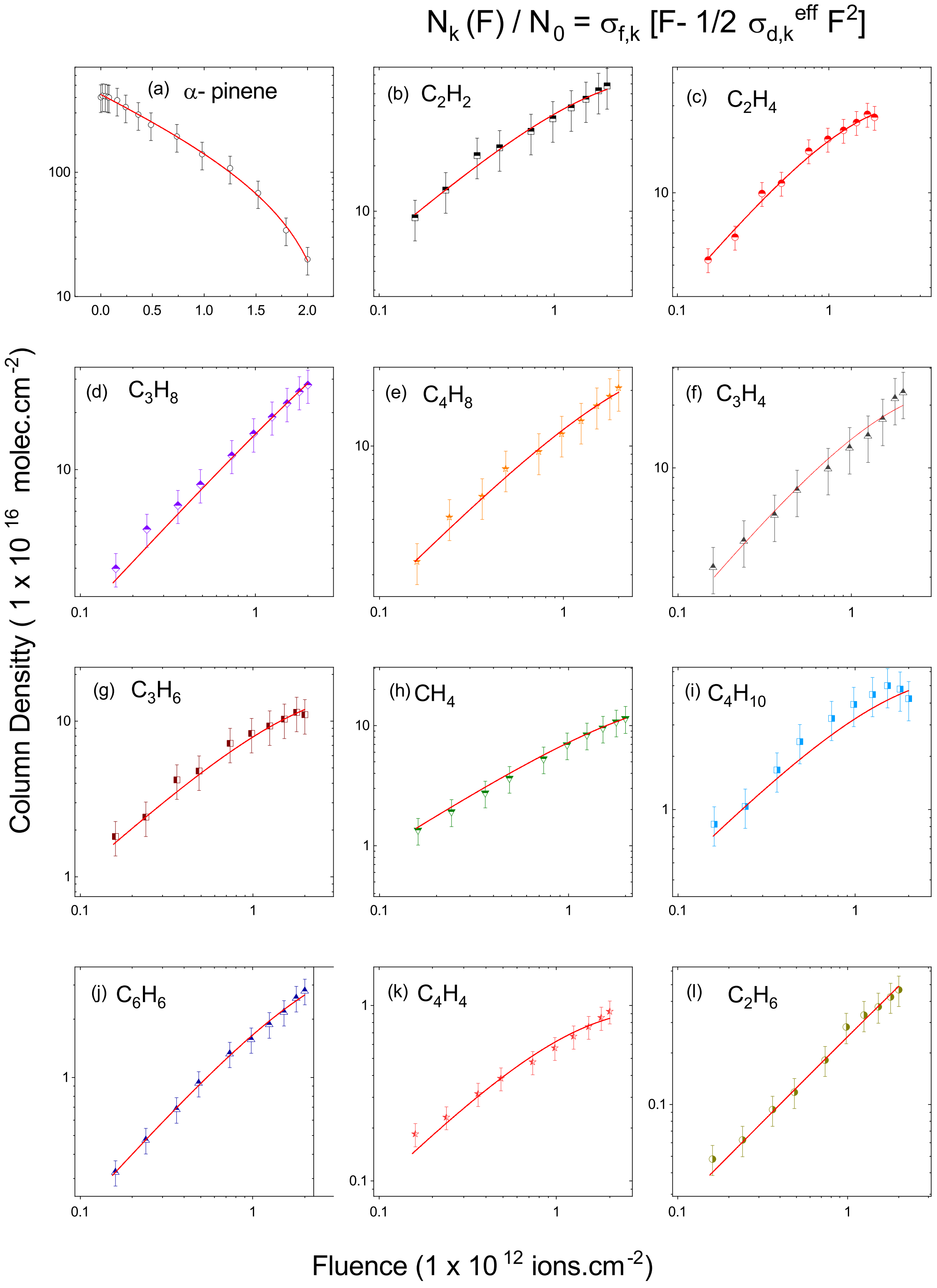

Figure 7. Column density evolution of α-pinene and the product species produced during radiolysis. Solid curves in red are fittings performed with Eq. (5) for the precursor and (6) for the products. (a) α-pinene, (b) acetylene (C_2H_2), (c) theethylene (C_2H_4), (d) propane (C_3H_8), (e) butene (C_4H_8), (f) propyne (C_3H_4), (g) propylene (C_3H_6), (h) methane (CH_4), (i) n-butane (C_4H_{10}), (j) benzene (C_6H_6), (k) vinylacetylene (C_4H_4), and (l) ethane (C_2H_6).

Table 5. Summary of carbon and hydrogen column density variations for α-pinene and the product molecular species. The bands used for the calculations are given in the second column. ΔN = ($N_f - N_0$), where N_f is final column density observed after the fluence of 2×10^{12} ions cm^{-2} and N_0 is equal to zero for all product species. The variation ΔN is expressed in $\times 10^{18}$ molecules cm^{-2}. The average destruction and formation yields in 10^6 molecules destroyed or produced per projectile are also given.

Species	Wavenumber (cm^{-1})	ΔN Carbon	ΔN Hydrogen	Yield Carbon	% Carbon	Yield Hydrogen	% Hydrogen
α-pinene $C_{10}H_{16}$	787.5	- 0.38	- 0.24	- 0.19	50.0%	- 0.12	50.0%
Produced	species*						
C_2H_2	3238.5	10	10	5	32.99%	5	40.3%
C_2H_4	3088.6	1.3	0.65	0.65	4.28%	0.33	2.62%
C_3H_8	752.4	0.9	0.34	0.45	2.98%	0.17	1.36%
C_4H_8	1643.1	0.5	0.26	0.26	1.73%	0.13	1.06%
C_3H_4	2125.1	0.8	0.58	0.38	2.53%	0.29	2.32%
C_3H_6	993.5	0.4	0.18	0.18	1.21%	0.09	0.074%
CH_4	1301.7	1.1	0.3	0.55	3.62%	0.14	1.1%
C_4H_{10}	955.2	0.1	0.04	0.05	0.33%	0.02	0.16%
C_6H_6	909.3	0.05	0.05	0.03	0.16%	0.03	0.20%
C_4H_4	1594.9	0.02	0.02	0.01	0.07%	0.01	0.09%
C_2H_6	2973.9	0.03	0.008	0.01	0.08%	0.004	0.034%
Total	-	15.2	12.4	7.6	50.0%	6.2	50.0%

*For molecules with more than one carbon and hydrogen atom, the corresponding atomic column density is obtained by multiplying the molecular column density by the number of carbon atoms plus hydrogen ones.

5 DISCUSSION

5.1 Radiochemical yield

The radiochemical effect is assumed to be linear with the stopping power, in the definition of radiochemical yield G. Nevertheless, examination of the values for G_f in Table 4 for Kr projectile indicates that they are dispersed over two orders of magnitude. This means that the energy transferred is not the only relevant quantity in molecular dissociation by fast ions.

The higher the stopping power, the greater the chemical modifications in the ice are expected to be. Accordingly, the formation cross-sections for products that were produced during irradiation of α-pinene ice in the current study (using a 61.3 MeV $^{84}Kr^{15+}$ beam) were expected to be higher than the cross-sections previously reported for 6 MeV $^{16}O^{2+}$, 220 MeV $^{16}O^{7+}$, 606 MeV $^{70}Zn^{26+}$, 267 MeV $^{56}Fe^{22+}$, and 40 MeV $^{58}Ni^{11+}$ beams (Mejía et al. 2013; de Barros et al. 2011a,b, 2016; Pereira et al. 2020). The results for formation cross-sections are shown in Fig. 10.

Although the ice concentrations are not equal, it is assumed that the law ($\sigma_{d,f} = a_{d,f}\ S_e{}^n$, where $n \sim 3/2$) still holds approximately. It is worth noting that this power law dependence was also reported by Godard et al. (2011) for aliphatic C-H hydrogenated carbons, by Mejía et al. (2013) for CH_4 irradiated with 6 MeV $^{16}O^{2+}$, 220 MeV $^{16}O^{7+}$, 267 MeV $^{56}Fe^{22+}$ and 606 MeV $^{70}Zn^{26+}$ and Mejía et al. (2013) for $H_2O{:}H_2CO{:}CH_3OH$ (100:2:0.8) ice mixture bombarded by 220 MeV $^{16}O^{7+}$ ions.

5.2 Carbon and hydrogen budget

The balance between the observed quantity of each atomic species still present in the sample as a function of fluence is known as the "atom budget." For the verification of whether the atomic column density of the destroyed α-pinene compound can account for the atomic column densities of the generated products, it is necessary to take into account each elemental budget.

The observed molecular column densities, precursor concentrations, and product stoichiometry are used to calculate the column density variations of the H and C atoms. They are contrasted with the starting amounts. Table 5 shows the carbon and hydrogen column density variations for α-pinene and the products molecules observed after irradiation (fluence of 2×10^{12} ions cm^{-2}).

Fig. 8(a) shows the evolution of the eleven product molecules column densities, $N_k(F)$. The label k corresponds to C_2H_2, C_2H_4, C_3H_8, C_4H_8, C_3H_4, C_3H_6, CH_4, C_4H_{10}, C_6H_6, C_4H_4, and C_2H_6. The total hydrogen (atoms.cm^{-2}) (green squares), total carbon (atoms.cm^{-2}) (red circles) and the ΔN_A (blue stars) are also taken into account in Fig. 8(a) and in Fig. 8(b) those values are compared with the carbon and hydrogen atoms of the precursor. Fig. 9 shows a comparison of the total carbon and hydrogen produced during irradiation.

The column densities N_A(F) for each one of the products were countably using Eq. (7):

$$N_A(F) = \sum_k n_{A,k} N_k(F), \tag{7}$$

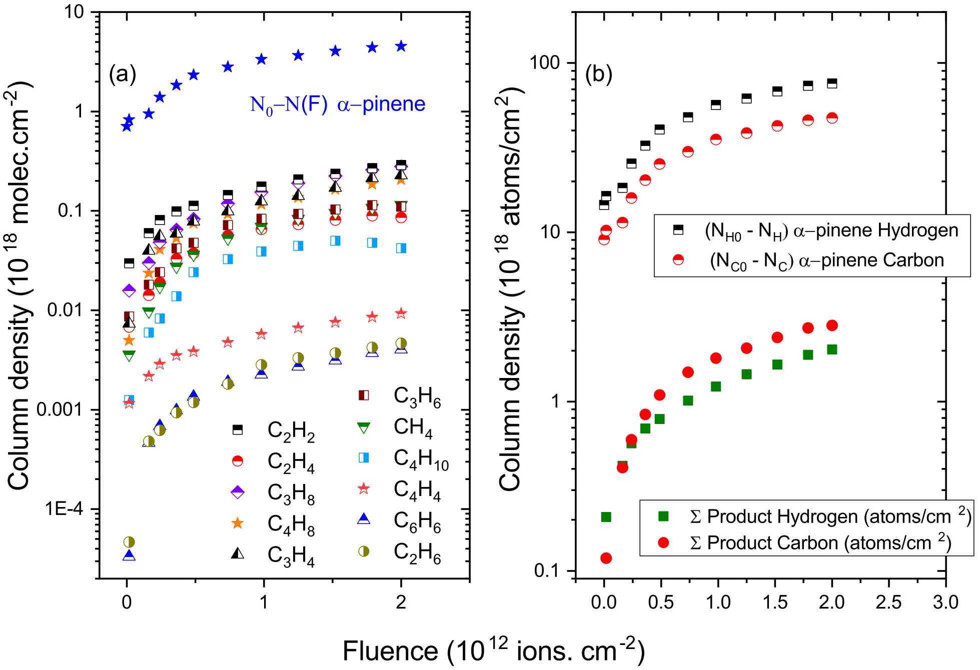

Figure 8. Comparison of the column density evolution as a funcion of ion fluence: (a) precursors dissociation and increase of product species, (b) evolution of hydrogen and carbon atoms from the dissociated precursor and from the products.

where $n_{A,k}$ is the number of atoms of the element A (A holds for carbon or hydrogen) in the produced molecule k. These data are compared with the atomic column density losses calculated for the α-pinene molecules, ΔN_A = $N_{0A,A}$ - N_A(F), where $N_{0A,A}$ is the initial value of N_A(F). These three functions are also plotted in Fig. 8(b).

The discrepancies between N_A(F) of Eq. (6) and ΔN_A allow the amount of unobserved material to be estimated and indicate possible inaccurate A-values. The percentages of carbon (50%) and hydrogen (50%) formed during irradiation were the same for carbon and hydrogen as can be seen in the last line of Table 4; that means that all the possible molecules that can be generated during the radiolysis of α-pinene are taking into account, and also that the A-values; used in our calculations are in excellent accuracy.

6 ASTROPHYSICAL IMPLICATIONS

The availability of chiral molecules on the prebiotic Earth has been well explained by (Bonner et al. 1979; Bonner & Liang 1984; Bonner 1995, 1999) employing a detailed scenario which involves the formation of such molecules on interstellar dust grains, followed by their transport to Earth. Bonner and co-workers highlighted the importance of homochirality and chiral homogeneity in modern biopolymers' self-replication, and the benefits of these chirality features in less complex polymeric systems are outlined based on experimental evidence. A brief review of chance and determinate abiotic mechanisms for the origin of chirality is given, along with their possible viability on the primordial Earth. The article emphasizes the impossibility of life without chirality and, consequently, of a biogenic scenario for the origin of chiral molecules. It is concluded that all such techniques would be impractical and that the continuous buildup of chiral compounds on primordial Earth would have required a continual alien source in the tumultuous prebiotic environment (Bonner 1999).

A scenario is presented in which the racemic components in the organic mantles on interstellar dust grains are photolyzed asymmetrically by the circularly polarized ultraviolet synchrotron radiation from the neutron star remnants of supernovae. This asymmetric photolysis results in the repeated transportation of these chiral constituents to the primordial Earth through either direct accretion of the interstellar dust or impacts by comets and asteroids (Bonner et al. 1979; Bonner & Liang 1984).

Theory explaining the formation of biological mantles on interstellar dust grains has been put forth by Greenberg (1984). According to his theory, ultraviolet light causes tiny interstellar molecules on dust grains to photolyze into free radicals that are then trapped and eventually recombine to create mantles containing bigger, even polymeric molecules. The radicals are then frozen as "ices" on the grains. Agarwal et al. (1986); Briggs et al. (1992) provided evidence for this theory by simulating the initial stages of the sequence in a lab setting, irradiating these frozen "ices" with ultraviolet light at 10 K, and creating artificial grain mantles that contained a variety of recognizable organic molecules, some of which were chirally capable.

Regarding amino acid radiolysis, noteworthy and traditional works by Bonner et al. (Bonner & Rubenstein 1987; Bonner & Lemmon 1978;

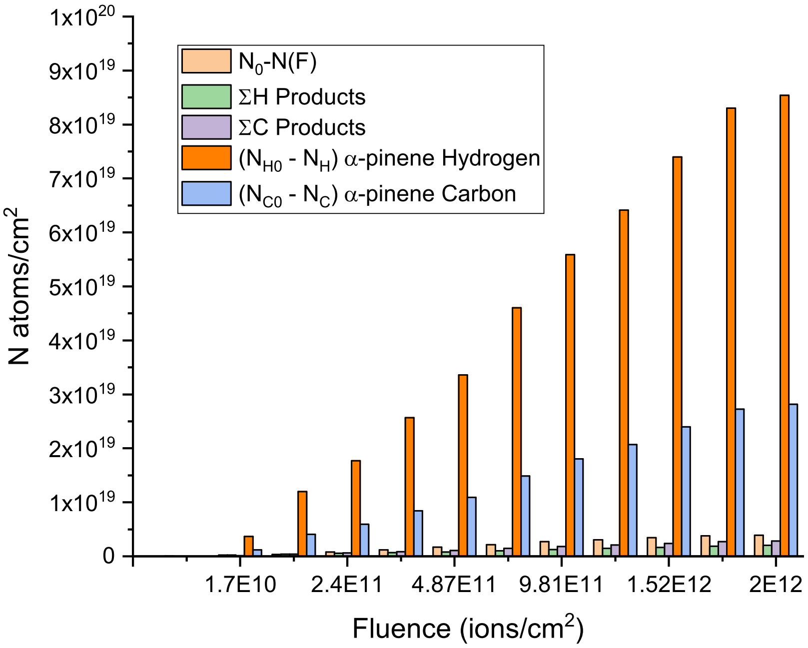

Figure 9. Comparison between the atomic column density evolution of product species and dissociated precursor as a function of ion fluence.

Bonner et al. 1979; Bonner & Liang 1984; Bonner 1999; Kminek & Bada 2006) are also accessible. These were performed especially to examine the Wester-Ulbricht hypothesis, which postulates that the origin of the enantiomeric excess in the biochemical world may be due to parity violation in the β-decay (Kminek & Bada 2006). Cataldo and co-workers (Cataldo & Ursini 2011; Cataldo et al. 2011a,b,c, 2013), have studied the higher energy radiation with chiral molecules, and more recent work of Costa et al. (2020) with 1.5 MeV H^+, He^+, N^+, and 230 MeV S^{+15} ion beams irradiating in valine lead the way to a comprehensive research on high energy radiation's impact on amino acids.

The finding that some meteorites, and carbonaceous chondrites in particular, are extraordinarily rich in molecules belonging to various classes of organic compounds and that the majority of them can be considered the ancestors or essential "building blocks" of the more complex molecules used for life is one of the most fascinating outcomes of astrochemistry and astrobiology (Anders 1991; Sephton 2002; Cronin & Pizzarello 2000; Martins & Sephton 2009; Glavin et al. 2010; Burton et al. 2012; Elsila et al. 2012; Cataldo et al. 2013).

The amino acids that are discovered in carbonaceous chondrites are among the many types of compounds that are found there, and they are quite important since some of them were found in racemic mixtures, most commonly with the L-enantiomer in modest excess (Pizzarello & Groy 2011). The fact that the amino acids present in meteorites are mostly not used by terrestrial biochemistry, making them entirely superfluous to the biosphere, is another trait that sets them apart from other amino acids (Cronin & Pizzarello 2000; Pizzarello & Groy 2000; Pizzarello et al. 2008; Martins & Sephton 2009). More specifically, the number of recognized amino acids in carbonaceous chondrites increased from 66 (Martins & Sephton 2009) to over 100 distinct molecular species (Pizzarello & Shock 2010; Burton et al. 2012) in a matter of years. But only a small portion of these amino acids—roughly 10% are now used by terrestrial biochemistry (Martins & Sephton 2009; Pizzarello & Shock 2010; Burton et al. 2012); the remaining amino acids are not engaged in protein synthesis because they are not encoded in DNA (Martins & Sephton 2009). This result is significant from a certain angle since it rules out the possibility that the carbonaceous chondrites studied by terrestrial life were contaminated; in that case, only the 21 terrestrial and proteinaceous amino acids would have been discovered.

The methyl esters of L-amino acids and their nitrosochlorides of natural monoterpene hydrocarbons, such as (+)-3-carene and (-)α-pinene, react to generate stereoselective hybrids of terpene-amino acids that are part of the α-substituted amino oxime series. Racemic DL-amino acid excesses and their derivatives cause the amino acid components to partially resolve in the process, forming diastereomeric mixes of terpene-amino acid hybrids with diastereomeric excesses ranging from 0 to 100% (Garcia et al. 2019).

Determining radiochemical yield (G-factor) and the cross-section dependence with stopping power is important as it allows a direct comparison with the known radiation effects produced by electrons, photons and ions. A comparison of our results (Table 4) with those of Gejvall & Lofroth (1975); Garrison et al. (1981) shows that they are consistent. They verified that release of ammonia leads necessarily to the formation of carboxylic acids with $G \sim 2.5$ molecules/100 eV and for the keto-acids $2.5 \geq G \geq 1.1$ (in molecules/100 eV). Table 6 displays the stopping power, dose for different projectiles and the values of the formation cross-sections obtained in this work and in the literature. In Fig. 10 the formation cross section of the products is plotted as a function of the stopping power.

According to Bonner (1999), radiolysis—the whole breakdown of the amino acid into smaller, achiral molecular fragments is the main

Table 6. Daughter species formation (σ_f) cross-sections in (10^{-15} cm^2) and S_e in eV/10^{15} molecules.cm^{-2}.

Projectile	E/m (MeV/u)	S_e	Dose (eV/molec)	Dose MGy	Exp. Target	C_2H_2	Formation C_2H_4	Cross CH_4	Section C_3H_8	C_2H_6	Ref.
6 MeV $^{16}O^{2+}$	0.38	491	11	58.9	CH_4	4.6	1.9	1.2^c	14	9.2	*a*
220 MeV $^{16}O^{7+}$	13.75	76.1	3.3	17.7	CH_4	2.2	0.15	1.4	0.06	1.2	*b*
16 MeV $^{16}O^{2+}$	1	650	7.7	41.3	CH_4	0.18	0.10	0.63	4.7	7.2	*a*
267 MeV $^{56}Fe^{22+}$	1	1136	17	91.1	CH_4	8.6	4.4	3.1^d	1.7	13	*a*
606 MeV $^{70}Zn^{26+}$	8.7	1040	12	64.3	CH_4	4.9	2.1	0.82^c	1.4	23	*a*
40 MeV $^{58}Ni^{11+}$	0.7	4633	54.7	110	C_2H_6:H_2O	21	3.0	1.6	1.3	30	*c*
40 MeV $^{58}Ni^{11+}$	0.7	3316	39.2	111	CH_4:H_2O	21	4.8	-	1.5	23	*d*
61.3 MeV $^{84}Kr^{15+}$	0.7	5769	31.9	22.6	$C_{10}H_{16}$	28	4.8	5.2	2.7	17	*e*
1 MeV H^+	1	28	0.3	1.1	C_2H_2	-	0.23	0.26	-	-	*f*

^{a}Mejía et al. (2013), ^{b}de Barros et al. (2011b), ^{c}de Barros et al. (2016), ^{d}Mejía et al. (2020) ^{e}This work, ^{f}Pereira et al. (2020).

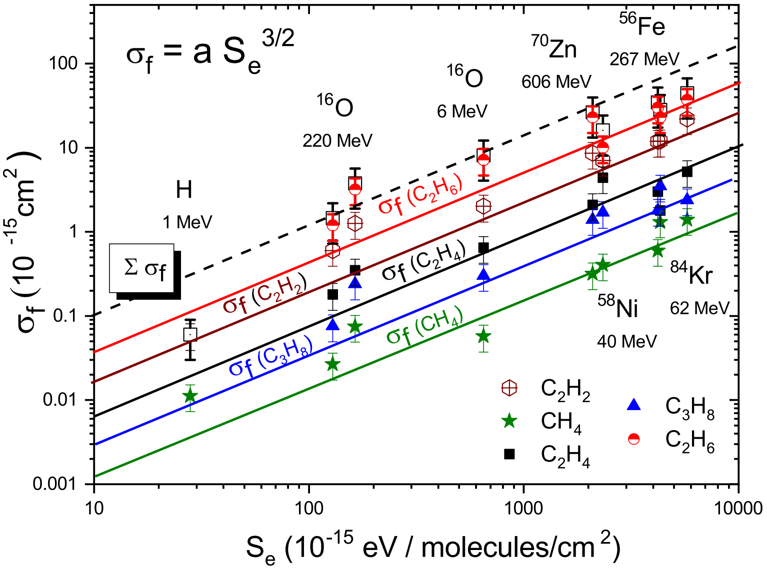

Figure 10. Dependence on formation cross-section of species: C_2H_2, C_2H_4, C_3H_8, CH_4 and C_2H_6 are plotted as function if electronic stopping power. Fittings (solid lines) refer to the function $\sigma_d \sim S_e{}^n$ with $n = 3/2$ for the current data. These results are compared with those presented in Table 6 for different projectiles and energies.

consequence of high energy radiation, and radioracemization of a chiral substrate at high radiation doses is only a secondary process. As a result, when chiral amino acids like L-2-Aminobutyric acid or D-2-Aminobutyric acid are exposed to radiation, they completely break down into small molecules NH_3, CH_4, H_2, CO_2, carboxylic, and keto acids. Since the loss of the molecules carrying the chiral center is what causes this chemical degradation, which is macroscopically shown as a reduction in the optical activity and in the Optical Rotatory Dispersion, we refer to it as a false or apparent radioracemization.

The solid state radiolysis of amino acids results in a number of fragmentation and also a some initial crystalline structure. The defects can be explained as a result of the amino acids molecular structure changing, which releases gaseous in our case, products like H_2, CH_4, and so on. In addition, new products like amines, amides, and carboxylic and keto acids are formed inside the crystalline structure, which naturally changes the crystal structure and acts as an impurity during the heating and melting process.

Multiple studies have been conducted over the past decades to understand the astrochemical processes leading to formation of C_nH_m molecules, such as α-pinene, during the irradiation can form routes with C_1 to C_6 hydrocarbons, the ones observed in our experimental procedures. Although a thorough analysis of the different pathways to small hydrocarbons available through these C_1 and C_2 precursors has been attempted, an isomer-specific study of the complex hydrocarbons that are formed deep within these ices from interaction with GCRs has been lacking until now. Therefore, all the hydrocarbon isomers detected in this work belong to a group in astrochemistry called complex organic molecules (COMs)—molecules having six or more atoms of carbon, hydrogen, nitrogen, and/or oxygen—which have been a key point of focus in recent years of laboratory astrophysics. Therefore, the main idea for those work, is to understand with our results how organic molecules—which are mostly destroyed in space by UV photolysis—behave when subjected to cosmic ray bombardment, such as the heavy ion simulation used in this work.

7 CONCLUSIONS

To our knowledge, there are only two α-pinene experiments at low temperature. Huang et al. (2018) investigated the chemical composition, size distributions, and degree of oligomerization of secondary organic aerosol (SOA) from α-pinene ($C_{10}H_{16}$) ozonolysis at 223 K. Ramachandran et al. (2022) carried out a the vacuum ultraviolet (VUV) photoabsorption measurements on pure molecular ices of isoprene and a few simple terpenes: limonene, α-pinene and β-pinene by forming icy mantles on cold dust analogs. From these experiments at low temperature (10 K), the VUV photoabsorption spectra of all the molecules reported here reveal similarities in the ice and gas phase as expected. Ramachandran et al. (2022) have proposed that isoprene and its oligomers, terpenes, along with other complex organic molecules, are expected to be present in the diverse environments of the ISM and in our solar system. We are not aware of any previous heavy ion radiation experiments of α-pinene.

Zhang et al. (2015) have identified monomers (C_{8-10} H_{12-16} O_{3-6}) oxidation products from one α-pinene molecule and dimers ($C_{14-19}H_{24-28}O_{5-9}$) oxidation products from two α-pinene molecules..

Our findings show that Kr ion irradiation of α-pinene ice lead to the formation of C_xH_y units, yielding small hydrocarbons including benzene (C_6H_6). The dissociation channels can be compared to those of polycyclic aromatic hydrocarbon molecules (PAHs) and adamantane molecules proposed to be present in young stars, but much more ubiquitous in the ISM (for example Candian et al. (2018); Ławicki et al. (2011)). Simular species have been also observed on Titan, particularly the aromatic benzene molecule, a central building block of molecules, and which is of crucial importance for the understanding of the organic chemistry of Saturn's largest moon (Coustenis & Hirtzig 2009; Hörst et al. 2012; Reynard & Sotin 2023).

During the irradiation process, the intensities of the α-pinene bands were observed and we tracked the development of the IR bands detecting the radiolysis products in relation to the fluence of irradiation. The laboratory α-pinene spectra are interpreted using theoretical data, which also aid in identifying the generated product bands. Understanding the α-pinene significance will help to comprehend the kind and abundance of biological molecules in space, as well as the need for knowledge regarding how long they will survive (or decomposition rates).

In this study, the production and destruction cross sections of the chemical molecules α-pinene are determined and the potential role of these compounds in relation to their produced products is investigated. The radiochemical yield determined should help to gain insight into the abundance of chiral molecules in space. The atom budget of the new twelve molecular species formed during irradiation re-enforced the conclusion that our theoretical A-values are precise. It is observed that C_2H_2, C_2H_4, C_3H_8, CH_4 and C_2H_6 formation cross-section dependence on electronic stopping power is described by the function $\sigma_d \sim {S_e}^n$ with $n = 3/2$ for the current data, in good agreement with other heavy ion experiment results.

ACKNOWLEDGMENTS

A L F de Barros and E F da Silveira acknowledge the Brazilian organizations CAPES, CNPq (Bolsa de Produtividade 307418/2021-9 and 30.4511/2022-6) and FAPERJ (E-26-210.965/2021, E-26-210.801/2021, E-26-245.307/2019, E-26-202.549/2019, E-26/201.934/2019, E-26-200.320/2023, and E-26/201.622/2023). We support by the Region Normandie (RIN SCHINOBI) including a post grant for CAPdC. The experiment was performed at Grand Accélérateur National d'Ions Lourds (GANIL) by means of CIRIL Interdisciplinary Platform, part of CIMAP laboratory, Caen, France.

8 DATA AVAILABILITY

The data underlying this article will be shared on reasonable request to the corresponding author.

REFERENCES

Abplanalp, M. J., & Kaiser, R. I. ,2020, The Astrophysical Journal, 889(1), 3.

Adhikary, A., Becker, D., & Sevilla, M. D., 2014, Applications of EPR in radiation research.

Agarwal, V. K, Schutte, W., Greenberg, J. M., Ferris, J. E, Briggs, R., Conner, S., van de Bult, C. E. E M., & Baas, E, 1986, Origins of Life 16, 2t.

An, P., Yuan, C. Q., Liu, X. H., Xiao, D. B., & Luo, Z. X. (2016). Vibrational spectroscopic identification of isoprene, pinenes and their mixture. Chinese Chemical Letters, 27(4), 527-534.

Anders, E., 1991, Space Science Reviews, 56, 157-166.

Andrade, D. P., de Barros, A. L., Pilling, S., Domaracka, A., Rothard, H., Boduch, P., & da Silveira, E. F., 2013, Monthly Notices of the Royal Astronomical Society, 430(2), 787-796.

Augé, B., Been, T., Boduch, P., Chabot, M., Dartois, E., Madi, T., Ramillon, J.M., Ropars, F., Rothard, H., Voivenel, P., 2018, Review of Scientific Instruments 89, 075105.

Bauschlicher, C. W., Ricca, A., Boersma, C., & Allamandola, L. J., 2018, The Astrophysical Journal Supplement Series, 234(2), 32.

Becke, A. D. , 1993, J. Chem. Phys., 98, 5648.

Bennett, C. J., Jamieson, C. S., Osamura, Y., & Kaiser, R. I., 2006, ApJ, 653(1), 792.

Bernstein, M. P., Cruikshank, D. P., & Sandford, S. A., 2005, Icar, 179(2), 527-534.

Bonner, W. A., 1991, Origins of Life and Evolution of the Biosphere, 21(2), 59-111.

Bonner, W. A., & Rubenstein, E., 1987, Biosystems, 20(1), 99-111.

Bonner, W.; Lemmon, R.M. Radiolysis, racemization, and the origin of optical activity. Bioorg. Chem. 1987, 7, 175–187.

Bonner, W.A.; Blair, N.E.; Lemmon, R.M.,1979, Orig. Life Evol. Biosph., 9, 279–290.

Bonner, W.; & Liang, 1984, J. Mol. Evol., 21, 84–89.

Bonner, W. A., 1995, Origins of Life and Evolution of the Biosphere, 25, 175-190.

Bonner, W.A.,1999, Radiat. Res., 152, 83–87.

Boogert, A. A., Gerakines, P. A., & Whittet, D. C., 2015, Observations of the icy universe. Annual Review of Astronomy and Astrophysics, 53, 541-581.

Bouilloud, M., Fray, N., Bénilan, Y., Cottin, H., Gazeau, M. C., & Jolly, A., 2015, MNRAS, 451(2), 2145-2160.

Briggs, R., Ertem, G., Ferris, J. P., Greenberg, J. M., McCain, P. J., Mendoza-Gomez, C. X., and Schutte, W.: 1992, Orig. Life EvoL Biosphere 22, 287.

Burton, A. S., Stern, J. C., Elsila, J. E., Glavin, D. P., & Dworkin, J. P., 2012, Chemical Society Reviews, 41(16), 5459-5472.

Candian, A., Bouwman, J., Hemberger, P., Bodi, A., & Tielens, A. G., 2018, Physical Chemistry Chemical Physics, 20(8), 5399-5406.

Cataldo, F., Brucato, J.R. & Keheyan, Y., 2007a, Biosph. 36, 477–485.

Cataldo, F., 2007b, Journal of Radioanalytical and Nuclear Chemistry, 272(1), 107-113.

Cataldo, F., 2007c, International Journal of Astrobiology 6 (1) : 1–10.

Cataldo, F., Ursini, O., Angelini, G., Iglesias-Groth, S., & Manchado, A., 2011a, Rendiconti Lincei, 22, 81-94.

Cataldo, F., Angelini, G., Iglesias-Groth, S., & Manchado, A., 2011b, Radiation Physics and Chemistry, 80(1), 57-65.

Cataldo, F., Ragni, P., Iglesias-Groth, S., & Manchado, A. 2011c, Journal of Radioanalytical and Nuclear Chemistry, 287(2), 573-580.

Cataldo, F., Lilla, E., & Ursini, O.,2011, Radiation Physics and Chemistry, 80(6), 723-730.

Cataldo, F., Iglesias-Groth, S., Angelini, G., & Hafez, Y., 2013, Life, 3(3), 449-473.

Cataldo, F.,& Iglesias-Groth, S. (2017). Radiation chemical aspects of the origins of life. Journal of Radioanalytical and Nuclear Chemistry, 311(2), 1081-1097.

Chen, D., Shao, H., Yao, W., & Huang, B., 2013, International Journal of Polymer Science, 2013.

Closs, A. C., Bechtel, M., & Trapp, O. 2022, Angewandte Chemie International Edition, 61, e202112563.

Closs, A. C., Fuks, E., Bechtel, M., & Trapp, O. 2020, Chemistry–A European Journal, 26, 10702.

Costa, C. A. D., Muniz, G. S. V., Boduch, P., Rothard, H., & Silveira, E. F. D., 2020, International journal of molecular sciences, 21(5), 1893.

Coustenis, A., & Hirtzig, M., 2009, Research in Astronomy and Astrophysics, 9(3), 249.

Cronin, J. R., & Pizzarello, S., 2000, Perspective in amino acid and protein geochemistry.

da Silveira, E. F., 2022, In Journal of Physics: Conference Series (Vol. 2340, No. 1, p. 012044). IOP Publishing.

de Barros, A. L. F., Domaracka, A., Andrade, D. P. P., Boduch, P., Rothard, H., & Da Silveira, E. F., 2011a, MNRAS, 418(2), 1363-1374.

de Barros, A. L. F., Bordalo, V. S. D. E., Duarte, E. S., da Silveira, E. F., Domaracka, A., Rothard, H., & Boduch, P., 2011b, Astronomy & Astrophysics, 531, A160.

de Barros, A. L. F., da Silveira, E. F., Fulvio, D., Rothard, H., & Boduch, P., 2016, ApJ, 824(2), 81.

de Barros, A. L. F., Mattioda, A. L., Korsmeyer, J. M., & Ricca, A., 2018, The Journal of Physical Chemistry A, 122(9), 2361-2375.

Darquié, B., Stoeffler, C., Shelkovnikov, A., Daussy, C., Amy-Klein, A., Chardonnet, C., ... & Saue, T., 2010, Progress toward the first observation of parity violation in chiral molecules by high-resolution laser spectroscopy. Chirality, 22(10), 870-884..

Duarte, E. S., Boduch, P., Rothard, H., Been, T., Dartois, E., Farenzena, L. S., & Da Silveira, E. F., 2009, A&A, 502(2), 599-603.

Duarte, E. S., Domaracka, A., Boduch, P., Rothard, H., Dartois, E., & Da Silveira, E. F., 2010, A&A, 512, A71.

Dunning Jr., T. H., 1989, J. Chem. Phys., 90, 1007.

Ehrenfreund, P., Bernstein, M. P., Dworkin, J. P., Sandford, S. A., & Allamandola, L. J., 2001, ApJ., 550(1), L95.

Ehrenfreund, P., Ruiterkamp, R., Peeters, Z., Foing, B., Salama, F., & Martins, Z.,2007, Planetary and Space Science, 55(4), 383-400.

Elsila, J. E., Charnley, S. B., Burton, A. S., Glavin, D. P., & Dworkin, J. P., 2012, Meteoritics & Planetary Science, 47(9), 1517-1536.

Frisch, M. J., Trucks, G. W., Schlegel, H. B., Scuseria, G. E., Robb, M., Cheeseman, J. R., ... & Fox, D. J., 2016, Gaussian 16, Revision A. 03, Gaussian. Inc., Wallingford CT, 3.

Garcia, A. D., Meinert, C., Sugahara, H., Jones, N. C., Hoffmann, S. V., & Meierhenrich, U. J., 2019, Life, 9(1), 29.

Gejvall, T.; Lofroth, G.,1975, Radiat. Eff., 25, 187–190.

Garrison, W.M., 1981, Radiat. Eff. 54, 29–40.

Glavin, D. P., Callahan, M. P., Dworkin, J. P., & Elsila, J. E., 2010, Meteoritics & Planetary Science, 45(12), 1948-1972.

Greenberg, J. M.: 1984, Sci. Am. 250, 124

Godard M., et al., 2011, A&A, 16228

Guijarro, A., & Yus, M., 2008, Royal Society of Chemistry.

Günay, B. Schmidt,T.W., Burton, M.G., Afsouar,M. Krechkivska, O., Nauta, K. S.H. Kable, A. Rawal, 2018, Mon. Not. R. Astron. Soc. 479 (4) 4336–4344.

Hadidi, R., Bozanic, D. K., Garcia, G. A., & Nahon, L.,2018, Advances in Physics: X, 3(1), 1477530.

Hörst, S. M., Yelle, R. V., Buch, A., Carrasco, N., Cernogora, G., Dutuit, O., ... & Vuitton, V., 2012, Astrobiology, 12(9), 809-817.

Huang, W., Saathoff, H., Pajunoja, A., Shen, X., Naumann, K. H., Wagner, R., ... & Mohr, C., 2018, Atmospheric Chemistry and Physics, 18(4), 2883-2898.

Hudson, R. L., Gerakines, P. A., Yarnall, Y. Y., & Coones, R. T., 2021, Icarus, 354, 114033.

Hudson, R. L., Gerakines, P. A., & Moore, M. H., 2014a, Icarus, 243, 148-157.

Hudson, R. L., Ferrante, R. F., & Moore, M. H.,2014b, Icarus, 228, 276-287.

Kaiser, R. I., & Roessler, K., 1998, ApJ, 503(2), 959.

Kim, Y. S., & Kaiser, R. I., 2009, The Astrophysical Journal Supplement Series, 181(2), 543.

Kim, Y. S., Bennett, C. J., Chen, L. H., O'Brien, K., & Kaiser, R. I., 2010, The Astrophysical Journal, 711(2), 744.

Kminek, G., & Bada, J. L., 2006, Earth and Planetary Science Letters, 245(1-2), 1-5.

Kramida, A., Ralchenko, Y., & Reader, J. (2012, June). Current status of atomic spectroscopy databases at NIST. In APS Division of Atomic, Molecular and Optical Physics Meeting Abstracts (Vol. 43, pp. D1-004).

Ławicki, A., Holm, A. I., Rousseau, P., Capron, M., Maisonny, R., Maclot, S., ... & Huber, B. A., 2011, Physical Review A, 83(2), 022704.

Lee, Y. C., Venkatesan, V., Lee, Y. P., Macko, P., Didiriche, K., & Herman, M., 2007, Chemical physics letters, 435(4-6), 247-251.

Martins, Z., & Sephton, M. A., 2009, Amino acids, peptides and proteins in organic chemistry: origins and synthesis of amino acids, 1, 1-42.

Mejía, C., de Barros, A. L. F., Bordalo, V., da Silveira, E. F., Boduch, P., Domaracka, A., & Rothard, H., 2013, MNRAS, 433(3), 2368-2379.

Mejía, C., De Barros, A. L. F., Rothard, H., Boduch, P., & Da Silveira, E. F., 2020, ApJ, 894(2), 132.

Muroya, Y., Plante, I., Azzam, E. I., Meesungnoen, J., Katsumura, Y., & Jay-Gerin, J. P., 2006,. Radiation research, 165(4), 485-491.

Nahon, L., Garcia, G., Powis, I., Meierhenrich, U., & Brack, A., 2007, In Instruments, Methods, and Missions for Astrobiology X (Vol. 6694, pp. 19-34). SPIE.

Pereira, R. C., de Barros, A. L. F., da Costa, C. A. P., Oliveira, P. R. B., Fulvio, D., & da Silveira, E. F., 2020, Monthly Notices of the Royal Astronomical Society, 495(1), 40-57.

Pizzarello, S., & Groy, T. L., 2011, Geochimica et Cosmochimica Acta, 75(2), 645-656.

Pizzarello, S., & Shock, E., 2010, Cold Spring Harbor perspectives in biology, 2(3), a002105.

Pizzarello, S., & Cronin, J. R., 2000, Geochimica et Cosmochimica Acta, 64(2), 329-338.

Pizzarello, S., Huang, Y., & Alexandre, M. R., 2008, Proceedings of the National Academy of Sciences, 105(10), 3700-3704.

Qiu, S., Li, G., Liu, P., Wang, C., Feng, Z., & Li, C., 2010, Physical Chemistry Chemical Physics, 12(12), 3005-3013.

Ramachandran, R., Pavithraa, et al., 2022, Spectrochimica Acta Part A: Molecular and Biomolecular Spectroscopy, 268, 120586.

Reynard, B., & Sotin, C., 2023, Earth and Planetary Science Letters, 612, 118172.

Ruiterkamp, R., Peeters, Z., Moore, M. H., Hudson, R. L., & Ehrenfreund, P., 2005, A&A, 440(1), 391-402.

Sephton, M. A., 2002, Natural product reports, 19(3), 292-311.

Stephens, P. J. , Devlin, F. J., Chabalowski, C. F. , Frisch, M. J.,1994, J. Phys. Chem., 98, 11623.

Strazzulla, G., & Baratta, G. A., 1991, Laboratory study of the IR spectrum of ion-irradiated frozen benzene. Astronomy and Astrophysics, 241, 310-316.

Tanabashi, M., Hagiwara, K., Hikasa, K., Nakamura, K., Sumino, Y., Takahashi, F., ... & Quadt, A., 2018, Review of particle physics. Physical Review D, 98(3), 030001.

Thakur, A. C., & Remsing, R. C., 2023, ACS Earth and Space Chemistry, 7(2), 479-489.

Tia, M., Cunha de Miranda, B., Daly, S., Gaie-Levrel, F., Garcia, G. A., Powis, I., & Nahon, L., 2013, The Journal of Physical Chemistry Letters, 4(16), 2698-2704.

Turner, J. E., Magee, J. L., Wright, H. A., Chatterjee, A., Hamm, R. N., & Ritchie, R. H., 1983, Radiation Research, 96(3), 437-449.

Z. Zhan, S. Seager, J.J. Petkowski, C. Sousa-Silva, S. Ranjan, J. Huang, W. Bains, Astrobiology 21 (7) (2021) 765–792.

Zhang, X., McVay, R. C., Huang, D. D., Dalleska, N. F., Aumont, B., Flagan, R. C., & Seinfeld, J. H., 2015, Proceedings of the National Academy of Sciences, 112(46), 14168-14173.

Zhou, L., Zheng, W., Kaiser, R. I., Landera, A., Mebel, A. M., Liang, M. C., & Yung, Y. L., 2010, ApJ, 718(2), 1243.

Ziegler, James F., M. D. Ziegler, and J. P. Biersack, 2010, NIMB 268, no. 11 (2010):1818-1823.